HHS Public Access

Author manuscript

ACS Nano. Author manuscript; available in PMC 2024 March 26.

Published in final edited form as:

ACS Nano. 2023 December 12; 17(23): 24154–24169. doi:10.1021/acsnano.3c09273.

Layer-by-Layer Polymer Functionalization Improves Nanoparticle Penetration and Glioblastoma Targeting in the Brain

Andrew J. Pickering[1,2], **Nicholas G. Lamson**[2], **Michael H. Marand**[2], **Wei Hwang**[2], **Joelle P. Straehla**[2,3,4,5], **Paula T. Hammond**[1,2,5,6,*]

[1]Department of Chemical Engineering, Massachusetts Institute of Technology, Cambridge, MA, 02142, USA

[2]Koch Institute for Integrative Cancer Research, Massachusetts Institute of Technology, Cambridge, MA 02142, USA.

[3]Department of Pediatric Oncology, Dana-Farber Cancer Institute, Boston, MA 02115, USA.

[4]Division of Pediatric Hematology/Oncology, Boston Children's Hospital, Boston, MA 02115, USA.

[5]Broad Institute of MIT and Harvard, Cambridge, MA 02142, USA.

[6]Institute for Soldier Nanotechnologies, Massachusetts Institute of Technology, Cambridge, MA 02139, USA.

Abstract

Glioblastoma is characterized by diffuse infiltration into surrounding healthy brain tissues, which makes it challenging to treat. Complete surgical resection is often impossible, and systemically delivered drugs cannot achieve adequate tumor exposure to prevent local recurrence. Convection-enhanced delivery (CED) offers a method for administering therapeutics directly into brain tumor tissue, but its impact has been limited by rapid clearance and off-target cellular uptake. Nanoparticle (NP) encapsulation presents a promising strategy for extending the retention time of locally delivered therapies while specifically targeting glioblastoma cells. However, the brain's extracellular structure poses challenges for NP distribution due to its narrow, tortuous pores and a harsh ionic environment. In this study, we investigated the impact of NP surface chemistry using layer-by-layer (LbL) assembly to design drug carriers for broad spatial distribution in brain tissue and specific glioblastoma cell targeting. We found that poly-L-glutamate and hyaluronate were effective surface chemistries for targeting glioblastoma cells *in vitro*. Co-adsorbing either polymer with a small fraction of PEGylated polyelectrolytes improved colloidal stability without sacrificing

*Correspondence to hammond@mit.edu.

Author Roles (Primary CRediT Role)
A.J.P. – Conceptualization
N.G.L. – Investigation
M.H.M. – Investigation
W.H. – Methodology
J.P.S. – Supervision
J.P.S. – Supervision

Supporting Information Available
Additional supporting figures for nanoparticle characterization, MRI imaging, histology and immunofluorescence, and flow cytometry data

cancer cell selectivity. Following CED *in vivo*, gadolinium-functionalized LbL NPs enabled MRI visualization and exhibited a distribution volume up to three times larger than liposomes and doubled the retention half-time up to 13.5 days. Flow cytometric analysis of CED-treated murine orthotopic brain tumors indicated greater cancer cell uptake and reduced healthy cell uptake for LbL NPs compared to non-functionalized liposomes. The distinct cellular outcomes for different co-layered LbL NPs provide opportunities to tailor this modular delivery system for various therapeutic applications.

Graphical Abstract:

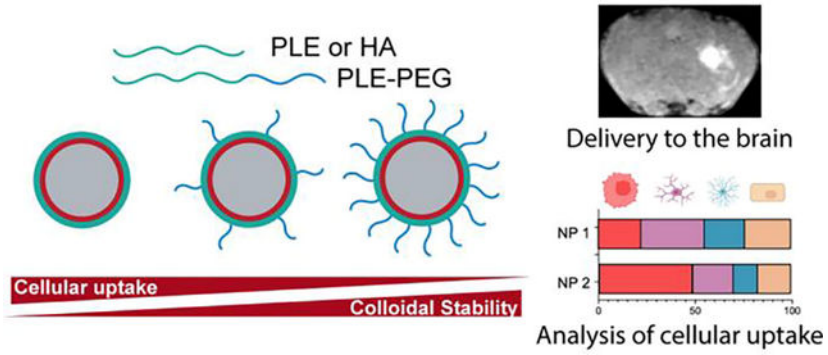

Keywords

Convection-enhanced delivery; nanoparticles; layer-by-layer; tumor penetration; cellular targeting; MRI imaging; glioblastoma

Glioblastoma, the most common primary malignant brain tumor, has seen limited treatment advancements over the past two decades.[1,2] The extensive infiltration of glioblastoma cells into surrounding, healthy brain tissue precludes complete surgical resection,[3] while the blood-brain barrier (BBB) prevents systemic therapies from reaching adequate levels in the brain.[4] Consequently, current treatment strategies only modestly extend median survival by 3–5 months.[5] Convection-enhanced delivery (CED) is an alternate strategy that bypasses the BBB by employing an applied pressure gradient to infuse therapies directly into the brain parenchyma.[6] Clinical trials have demonstrated its safety and feasibility, achieving effective local drug concentrations with minimal systemic toxicity.[7–9] However, locally administered free drugs are cleared rapidly from the brain and can be toxic to nearby off-target cells, highlighting the need for alternate drug carriers.[10–12]

Nanoparticles (NPs) present a promising approach to improving the retention and cellular targeting of locally administered therapies via control over vehicle size and surface chemistry.[13,14] To effectively treat invasive tumors such as glioblastoma, NPs must penetrate the narrow pores of the brain extracellular space (ECS), estimated to be below 100 nm in tumor tissue,[15] although recent findings suggest up to a quarter of pores may exceed this size.[16] The brain's ECS nonetheless poses unique challenges to the widespread distribution of NPs. The extracellular fluid has a high ionic strength with millimolar levels of Ca^{2+}, which can promote NP aggregation, limiting the distribution of NPs that can meet these

size restrictions in other biological fluids.[17] Additionally, the dense anionic network of extracellular matrix can lead to nonspecific binding with NPs, further reducing their mobility.[18] Given these challenges, most translational NPs have focused on antifouling surfaces, such as polyethylene glycol (PEG), which provide colloidal stability and reduce non-specific interactions with the anionic extracellular matrix. While such coatings enable widespread distribution in the brain,[19] they simultaneously limit NP recognition by cancer cells, preventing the targeted internalization of their payload.[20,21]

Several strategies have been explored to enhance the cellular targeting of NPs delivered by CED. Traditional covalent conjugation of antibodies or cationic peptides may compromise size and colloidal stability, often leading to a limited surface presentation of ligands.[22,23] Another strategy employed for local delivery is bioadhesive polymers; for example, aldehyde groups on poly(lactic acid) NPs have been shown to increase internalization by all cell types *in vivo* without compromising brain penetration.[20] However, due to the diffuse invasion of glioblastoma into healthy tissues, locally infused NPs will encounter a mixed population of tumor and healthy cells, and cancer-cell specificity may improve the therapeutic index of anti-cancer agents.[24] There remains a need to investigate other NP surface chemistries that can address the competing considerations of extracellular distribution and glioblastoma-specific cellular targeting.

The layer-by-layer (LbL) assembly method provides a modular approach for modifying the surface chemistry of charged colloidal substrates.[25] Through the sequential adsorption of polyelectrolytes of opposite charge onto the NP surface, LbL modification can be applied to a variety of well-characterized NP cores, including poly(lactic-co-glycolic) acid,[26] quantum dots,[27] and liposomes;[28] among these, liposomes are currently undergoing clinical trials for CED.[29] The LbL approach enables rapid exploration of a broad range of outer surfaces composed of natural or synthetic polyelectrolytes.[30,31] Importantly, the high weight loading of polyelectrolytes can increase multivalent interactions between the outermost layer and receptors on the surface of cancer cells, for example, between sodium hyaluronate and CD44, leading to increased uptake.[32] While LbL holds promise for designing NP surfaces for CED, ensuring colloidal stability while retaining cellular specificity in the harsh ionic environment of the brain remains a critical obstacle to overcome.

In this study, we examine the impact of NP surface chemistry using LbL assembly toward designing drug carriers with broad spatial distribution in the brain and selective targeting of glioblastoma cells. We investigated two distinct outer layers, poly-L-glutamate and hyaluronate, which we demonstrate to have high uptake by glioblastoma cells. To maintain colloidal stability under physiological conditions, we developed a co-layering strategy using a minimal amount of PEGylated polyanion block copolymer and systematically adjusted the outer layer composition to balance stability with cellular targeting. Using a variety of patient-derived glioblastoma models with different media compositions and growth formats, we show that co-layered LbL NPs maintain high glioblastoma association, selectivity, and spheroid penetration *in vitro*. To test whether co-layered LbL NPs can penetrate brain tissue, we functionalized NPs with gadolinium for MRI visualization and performed CED in healthy and tumor-bearing mice. LbL NPs demonstrated up to a threefold increase in the volume of distribution compared to non-functionalized liposomes, with a doubled

retention half-time of approximately 13 days. To assess tumor cell targeting and specificity, we performed flow cytometry on dissociated mouse brains and examined NP association with 8 common cell types using flow cytometry. Co-layered LbL NPs displayed increased specificity for tumor cell uptake, with distinct cell type distributions for different outer layers. This approach provides insights into the cellular fate of surface-functionalized NPs in the brain, defining a set of criteria for the development of targeted local therapies for glioblastoma.

Results and Discussion

Synthesis and characterization of co-layered LbL NPs

Using ~90 nm fluorescently tagged anionic liposomes as cores, we prepared LbL NPs by adsorbing an initial polycation layer of poly(L-arginine hydrochloride) (PLR, 38 kDa), followed by a polyanion outer layer. We first prepared a library of 22 LbL NPs by employing a range of both naturally occurring and synthetic outer layer polyanions, encompassing carboxylated and sulfated surface chemistries (Figure S1A). We used flow cytometry to assess NP-cell associations using patient-derived GBM22 glioblastoma and identified the outer layer polyanions poly(L-glutamic acid sodium salt) (PLE, 15 kDa) and sodium hyaluronate (HA, 20 kDa) as having the highest overall glioblastoma cell association (Figure S1B). PLE, a synthetic polypeptide, has been shown to increase the targeting of LbL NPs to ovarian cancer cells by a combination of specific and non-specific binding mechanisms, though the precise mechanism remains unclear.[30] HA, a polysaccharide present in the brain extracellular space, is a ligand of the CD44 receptor, which is overexpressed in glioblastoma.[33] Given their strong association with GBM22 cells, we hypothesized that the outer layer polyanions PLE and HA could enhance glioblastoma targeting after local delivery, with their differing structures and origins possibly suggesting distinct mechanisms and applications.

We next investigated the colloidal stability of LbL NPs in artificial cerebrospinal fluid (aCSF) to mimic the conditions of the brain parenchyma. When incubated in DI water, both PLE and HA LbL NPs had a Z-average diameter of approximately 110 nm, a polydispersity index below 0.2, and a negative zeta potential that exceeds −30 mV. However, when incubated in aCSF at 37 °C overnight, both NPs aggregated, reaching Z-average diameters above 500 nm (Figure 1A). This observation underscores a challenge posed by the brain environment, where high ionic strength and limited protein content contribute to LbL NP instability by shielding electrostatic charges and promoting particle bridging.[34] As expected, LbL NPs with an outer layer of PLE-b-PEG5k maintained colloidal stability in aCSF after overnight incubation at 37 °C. Surface PEGylation is known to enhance colloidal stability via steric repulsions at the expense of limiting interactions with all cell types.[20,30]

To retain the cellular targeting properties of PLE and HA while also ensuring colloidal stability in aCSF, we developed a co-layering strategy incorporating block copolymer PLE-PEG (Figure 1B) in conjunction with the polyanion layer. Keeping the total polyanion:core ratio fixed at 1 weight equivalent, we varied the ratio of either PLE with PLE-PEG in the layering buffer. As the ratio of PLE-PEG to PLE increased, the zeta potential of the purified NPs increased from −45 mV to −30 mV, attributable to the neutral polymer blocks

(Figure 1C, raw DLS profiles shown in Figure S2). We show that a minimum of 40% (w/w) PLE-PEG in the outer layer is needed to maintain colloidal stability in aCSF, as defined by a <10% increase in the z-average diameter after overnight incubation at 37 °C. Owing to the high charge density and low persistence length of PLE, we hypothesized that PLE-PEG could stably adsorb onto LbL NPSs when co-layered with other, less densely charged polyanions. By co-layering PLE-PEG and HA, we found that 40% (w/w) PLE-PEG in the outer layer is needed to maintain colloidal stability in aCSF (Figure 1D). We further validated our co-layering approach using fluorescently-tagged PLE-Cy3, HA-Cy3, and PLE-PEG-Cy7. Both PLE and PLE-PEG were retained on the purified NPs in approximately the same weight ratio as was added to the layering buffer solution (Figure S3A, B). In contrast, HA was present in higher amounts on the particles relative to its buffer ratio, likely due to the lower charge density, requiring a larger amount of polymer to match the net charges on the polycation layer (Figure S3C). Self-associative properties of hyaluronan that involve other secondary interactions may also play a role in the higher mass ratio of HA adsorbed versus that in the buffer.[35] Results from both outer layer types indicate that colloidal stability can be achieved while PLE or HA comprise the majority of the outer layer by weight.

We next sought to investigate how the incorporation of surface PLE-PEG impacted cancer cell associations. Using flow cytometry, we studied the associations between GBM22 cells and fluorescently tagged liposomes and LbL NPs with varying degrees of PLE-PEG co-layering, following a 24-hour incubation period. As expected, NP-associated fluorescence decreased for both PLE and HA formulations as the proportion of PLE-PEG in the outer layer increased (Figure 1E). A one-way ANOVA indicated significant differences in NP-associated fluorescence among the PLE and HA formulations groups (raw data shown in Figure S4). In both cases, adding PLE-PEG beyond 40% (w/w) continued to reduce NP association, suggesting a diminishing benefit when incorporating more PLE-PEG than necessary for colloidal stability in aCSF. Together, these results show that co-layered LbL NPs featuring either PLE or HA surface chemistries can be stable in aCSF and demonstrate tunable degrees of cellular uptake that exceed that of core liposomes.

Co-layered LbL NPs maintain preferential interactions with glioblastoma cells.

To more comprehensively characterize the effects of co-layering PEGylated polymers on NP-glioblastoma cell selectivity, we prepared a library of PLE and HA-based LbL NPs using PLE-PEG fractions of 0%, 40%, and 100% (w/w). For comparison, we also tested the interactions of liposome cores and PEG-liposomes containing 0.6% (mol/mol) 18:0 PE-PEG5k to match the approximate PEG density and molecular weight of PLE-PEG LbL NPs. (Figure 2A). All NPs had similar Z-average diameters below 130 nm and PDIs below 0.2, with all except PLE and HA exhibiting colloidal stability in aCSF (Figure S5). We evaluated the NP-cell associations using flow cytometry after 4 or 24-hour incubations with a panel of 4 patient-derived glioblastoma cell lines (GBM22, E57, E21, and BT145) and 4 noncancerous neural cells (primary human astrocytes, endothelial cells, pericytes, and immortalized HCM3 microglia). To enable visualization and comparison of the relative uptake of each NP by different cell lines, the NP-associated fluorescence for each formulation was Z-scored (Figure 2B, with raw data in Figure S6). Hierarchical clustering revealed that all LbL formulations preferentially associated with glioblastoma

cells over noncancerous cells, with the effect amplified after 24 hours. This pattern was not observed with liposome cores or PEG-liposomes, which demonstrated comparable interactions with astrocytes and endothelial cells to those with cancer cells, even after 24 hours.

To further investigate glioblastoma specificity over noncancerous neural cells, we plotted the overall NP-cell associations using the aggregated data from individually tested cancer cell lines versus noncancerous cell lines. PLE and HA LbL NPs with 0% PLE-PEG demonstrated the highest specificity toward cancer cells at 24 hours, with 4.3 and 3.1-fold specificity, respectively (Figure 2B, bottom plots). This is in line with previous studies on LbL NPs that have highlighted the importance of carboxylate density and ligand-binding capacity for cancer cell selectivity.[30] Incorporating anti-fouling PEG chains can shield these interactions, reducing cancer specificity. As expected, co-layered PLE and co-layered HA NPs, hereafter referred to as co-PLE and co-HA, had intermediate specificities (3.0-fold and 2.6-fold, respectively), while 100% PLE-PEG NPs exhibited the lowest specificity among LbL formulations (2.4-fold).

To investigate whether PLE chains in co-layered LbL NPs remain accessible for interaction with cell surface receptors, we performed a two-step blocking experiment. First, we pre-treated E57 glioma cells with high molecular weight PLE (120 kDa) to saturate any PLE-specific cell membrane receptors. We subsequently incubated the cells with NPs for 2 hours and quantified the NP-associated fluorescence with flow cytometry. PLE blocking had no observed effect on the association of liposomes; however, we noted a 50% reduction in PLE NP association ($p = 0.001$), a 28% reduction in co-PLE NP association ($p = 0.15$), and a 21% reduction in PLE-PEG NP association ($p = 0.38$) (Figure 2C). This trend indicates a diminishing capacity for PLE chains to interact with cell membranes with increasing PEG densities, with co-PLE NPs trending towards interacting to a greater extent than PLE-PEG NPs. We conducted a similar experiment for HA NPs by blocking with exogenous high molecular weight HA (100 kDa), known to bind CD44 among other membrane receptors on glioma cells.[36] HA blocking significantly reduced the cellular associations of both HA and co-HA formulations by 47% ($p = 0.004$) and 25% ($p = 0.036$), respectively, while liposomes and PLE-PEG NPs remained unaffected (Figure 2D). These findings suggest that PLE-PEG co-layering provides a strategy for incorporating distinct surface chemistries with cancer-cell-specific affinity while preserving their specific cell-membrane binding interactions.

Having demonstrated a high degree of association and specificity with glioblastoma cells, we next visualized the cellular uptake of NPs by GBM22 cells using confocal microscopy. Consistent with flow cytometry results, we observed minimal NP fluorescence in cells treated with unfunctionalized or PEGylated liposomes compared to all LbL formulations (Figure 2E, additional replicates in Figure S7). Staining cell membranes with wheat germ agglutinin revealed that outer layer composition affects cellular internalization. LbL NPs with an outer layer of PLE showed a high degree of membrane association after 24 hours of incubation, consistent with previous studies with ovarian cancer cells.[30,37] In contrast, co-PLE NPs were mainly present in the cytoplasm. Intracellular delivery is necessary for many classes of anti-cancer therapies; thus, a modest reduction in overall association caused by

co-layering with PLE-PEG may be offset by increased internalization. PLE-PEG co-layering did not significantly alter the high internalization efficiency of HA NPs.

Co-layered LbL NPS penetrate glioblastoma spheroids.

We next hypothesized that co-layered LbL NPs would improve the penetration and uptake of LbL NPs into dense, 3-dimensional cellular structures due to their high colloidal stability and cellular targeting. We developed a flow cytometry-based assay to assess both penetration and cellular uptake into ~250 μm diameter BT145 glioblastoma spheroids, quantifying the fraction of NP-positive cells and the NP-associated fluorescence after 4 hours of incubation (Figure 3A). PEGylation reduced uptake and penetration for liposomes. For both PLE and HA NPs, co-layering with 40% PLE-PEG reduced NP-associated fluorescence, consistent with the results of 2-dimensional assays, yet the fraction of NP-positive (NP+) cells increased (Figure 3B). NPs with an outer layer of 100% PLE-PEG exhibited reduced penetration and overall uptake compared to co-layered NPs. These data suggest that PLE-PEG co-layering can improve the uniformity of NP distribution within dense 3D structures while preserving some of the cellular targeting properties.

To validate these findings and visualize the extent and uniformity of NP penetration, we conducted confocal microscopy on cryosectioned spheroids incubated with NPs for 24 hours. PLE NPs exhibited a bright outer ring of NP fluorescence with minimal signal in the spheroid core, indicating that only the outermost layer of cells took up NPs (Figure 3C). This observation is consistent with the smaller fraction of NP+ cells detected with the flow cytometry assay. By plotting the radially integrated fluorescence intensity versus distance, we found that co-PLE NPs have a more uniform distribution with a higher NP signal in the spheroid core compared to PLE (Figure 3D). This finding may be due to the high cell membrane-affinity interactions of PLE NPs, which are partially shielded when co-layered with PLE-PEG. HA NPs exhibited higher penetration into the spheroid core than PLE NPs, potentially aided by more efficient cellular internalization, which was maintained when co-layering with PLE-PEG (Figure 3E, F). Based on these findings, we investigated co-layered NPs with 40% (w/w) PLE-PEG as colloidally stable, cell-targeting NPs for CED *in vivo*.

Gadolinium-functionalization for MRI imaging

To provide a live imaging modality for *in vivo* studies, we incorporated a gadolinium-chelated lipid, 18:0 PE-DTPA(Gd), into the liposome bilayer for MRI contrast (Figure 4A Schematic).[38,39] CED is often performed with co-infusion of a separate gadolinium-based MRI contrast agent to visualize the volume of distribution non-invasively over time; however, NPs may distribute significantly differently from small molecular chelates.[29] Thus, stable incorporation of a Gd into the liposome core was critical in our studies to evaluate the distribution of the drug carrier itself.[12] We prepared Gd-functionalized liposomes by replacing 5 mol% 18:0 PE with 18:0 PE-DTPA(Gd), resulting in a Gd concentration of 0.075 mM in a 1 mg/mL liposome solution as determined by inductively coupled plasma mass spectroscopy. T1-weighted (T1W) MRI of Gd-functionalized liposomes, co-PLE, and co-HA NPs at various concentrations *in vitro* showed concentration-dependent T1 hyperintensity (Figure 4A). We further characterized the T1 relaxivity of different

formulations by calculating the slope of the linear T1 relaxation time versus the NP concentration (Figure S8A). There were no significant differences in relaxivity, indicating that the presence of highly hydrated polyelectrolyte layers does not restrict the availability of water molecules interacting with Gd presented on the outer and inner surface of the liposome bilayer. Thus, modification of the liposome core with Gd allows for direct comparison between LbL and unlayered formulations. Importantly, Gd-functionalized liposomes and LbL NPs had a similar size and zeta potential as NPs without Gd, and we confirmed the GBM22 glioblastoma cellular uptake was unaffected by the presence of Gd (Figure S8B, C).

LbL NPs improve the volume of distribution (V_D) and retention in healthy mice.

We performed CED (CED) in healthy, Ncr nude mice using gadolinium-modified fluorescent liposomes, co-HA, and co-PLE NPs. 24 hours after infusion, all NP formulations showed clear T1 MRI contrast in the injection site (Figure 4B, top row). Coronal-matched cryo-fluorescence images of the same brains show close agreement between the distribution of fluorescent and gadolinium-labeled lipid components (Figure 4B, bottom row). Colocalization of T1 contrast with BDP650/665 fluorescence, which is conjugated to a different lipid, confirms that MRI tracks the NPs, not free gadolinium. Segmentation of the 3D region of T1 hyperintensity revealed that LbL NPs have higher volumes of distribution than liposomes (Figure 4C). The volume of distribution to volume of infusion ratio (V_D/V_I) is 1.5 for PLE-co NPs, 1.0 for HA-co NPs, and 0.46 for liposomes. V_D/V_I ratios of 1–2 have been reported in rodents for several other nanocarrier formulations for CED with similar sizes and are an indicator of particularly promising CED systems.[20,40–42]

We subsequently assessed the retention of NPs in the brains of healthy mice. As controls, we injected free Gadavist (MW: 604.7 Da) and Galbumin (gadolinium-labeled albumin, MW: ~74 kDa) at doses with equivalent gadolinium content, representing unencapsulated low and high molecular weight drugs, respectively. Free Gadavist was presumably cleared from the brain within hours, as only minimal MRI signal could be observed 4 hours after infusion (Figure S9). Galbumin showed the largest V_D/V_I of 2.2 at 4 hours, but significantly decreased by 24 hours, with a V_D/V_I of only 0.4. In contrast, all NP formulations showed T1 contrast for at least 14 days, with T1 contrast remaining detectable at 21 days for co-LbL groups (Figure 4D). Pilot experiments showed no significant differences in NP distribution between 4-hour and 24-hour time points for all nanoparticle formulations (Figure S9). Due to limited MRI access and prolonged intracranial surgeries, 4-hour imaging was specifically prioritized for groups with rapid clearance. A retention half-time for each formulation was calculated from an exponential fit of the time-dependent V_D/V_I and was 11.5 hours for Galbumin, 6.5 days for liposomes, 12.1 days for co-HA NPs, and 13.5 days for co-PLE NPs (Figure 4E). These data are particularly relevant because NPs that remain localized to the injection site for several weeks could provide sustained exposure to encapsulated therapeutics and decrease the frequency of CED infusions. Several active liposomal drug loading strategies have been developed that provide a potential therapeutic rationale for prolonged retention. For example, liposomal irinotecan and doxorubicin have demonstrated release profiles spanning several days.[43,44] Notably, the sustained presence of gadolinium-chelated lipids observed throughout the study duration suggests that conjugation of the

therapeutic to the liposome core may be a promising approach and has been previously applied to LbL systems.[37]

No behavioral signs of neurological toxicity were observed in any mice throughout the 3-week retention study, and there were no significant differences in weight between any NP groups or a dextrose control (Figure S10A). Brain tissues were processed for histological analysis three days or three weeks after infusion to further evaluate the short-term and long-term toxicity of different formulations. Three days after infusion, all groups showed evidence of trauma along the needle tract, and several samples showed microhemorrhages, which we attribute to the moderate likelihood of damaging major blood vessels during the CED surgeries in rodents (Figure S10B).[20,45] Three weeks after infusion, most needle trauma has resolved, but we observed some degree of focal necrosis in all NP groups, suggesting concentration-dependent toxicity (Figure 4F). However, the degree of necrosis in co-LbL groups appears to be less severe than the unmodified liposome core, a result that aligns with *in vitro* toxicity with astrocytes (Figure S10C). In line with our data, liposomal-based systems have been previously shown to be non-toxic in CED applications and have advanced to human clinical trials.[29,46] The additional polymeric materials used for LbL functionalization have been characterized in a range of therapeutic applications and delivery routes.[27,47] Elucidating the clearance mechanism and metabolism of LbL NPs within the brain will be central to future therapeutic applications.

LbL NPs improve V_D and tumor targeting in mice with intracranial tumors.

CED is often performed in unresectable, invasive tumors or at the margins of a resection cavity where both tumor cells and healthy cells are intermingled.[48] To replicate these conditions, we inoculated mice with intracranial tumors using the highly invasive patient-derived BT145-luc glioblastoma cell line.[49] Approximately 100 days after inoculation, dense tumors formed with extensive invasion throughout the striatum, and substantial populations of healthy astrocytes, neurons, and microglia were present in the tumor bulk and periphery (Figure S11). Mice were randomized into three treatment groups (liposome, co-HA, and co-PLE) based on the tumor volume assessed by IVIS bioluminescence and T2-weighted (T2W) MRI (Figure S12). 24 hours after CED, performed in the same coordinates as tumor implantation, all NP types showed T1W MRI contrast in approximately the same region as the tumor hyperintensity from T2W scans acquired before infusion (Figure 5A, top two rows). Coronal-matched fluorescent images of the same brains show close agreement between the T2W tumor signal and T1 NP contrast, with human GBM nuclei shown in green and NPs shown in the “red hot” LUT (Figure 5A bottom row). Concordant with data in healthy mice, the PLE- and HA-co NPs had higher volumes of NP distribution than non-functionalized liposomes (V_D/V_I of 1.4 for PLE-co NPs, 1.3 for HA-co NPs, and 0.7 for liposomes, Figure 5B). Volumes of distribution show higher variability in tumor-bearing mice, likely due to differences in tissue architecture and cell density.

We next assessed the cellular associations of NPs *in vivo*. 24 hours after CED, brains were removed and processed for live-cell flow cytometry using the Miltenyi Adult Brain Dissociation Kit (Figure 5C). By setting a NP fluorescence gate for all live cells based on the untreated hemisphere, we observed a similar percentage of NP+ cells across the three

NP groups. Specifically, 8.4% of live cells were NP-positive with liposomes, 11.1% for co-HA, and 11.3% for co-PLE. This was initially surprising, as *in vitro* studies showed that both LbL formulations had significantly higher associations with all cell types. We further examined NP association with specific cell types by staining with surface markers for lymphocytes, myeloid cells, microglia, endothelial cells, astrocytes, oligodendrocytes, and pericytes in addition to human tumor cells (Figure S13 A,B). When examining tumor cells, we found that 8.4% were associated with liposomes, while 15.3% were associated with co-HA NPs and 18.0% with co-PLE NPs (Figure 5D). We noted through immunofluorescence examination a significant invasion of cancer cells throughout the corpus callosum, the largest white matter tract in rodents. We hypothesize that partial tumor cell coverage (as inferred by percent NP-positive tumor cells) is due to the extensive invasion of tumor cells throughout the parenchyma, particularly along the corpus callosum. NP injection sites were explicitly planned to avoid the corpus callosum, as it can act as a path of least resistance to divert a large fraction of NPs and influence the calculation of V_D/V_I.[45]

We further examined the cellular composition of the dissociated hemispheres (Figure 5E). The population of unstained cells likely includes neurons, which do not have a reliable exclusive surface marker, and a small fraction of other unstained cells. In all NP treatment groups, tumor cells made up approximately 20% of cells in the treated hemisphere. Microglia comprised the largest portion of recovered live cells overall, followed by astrocytes, oligodendrocytes, and unstained cells in roughly equal proportions. While brain dissociation procedures are complex and cannot easily be compared between separate studies, this cellular composition aligns with other studies using similar methodology and gating strategies.[50,51] We then assessed the cellular composition of NP-positive cells by applying the same cell-type gating strategy to the NP+ fraction. (Figure 5F). The cellular composition of liposome-positive cells was similar to the overall cellular distribution in the treated hemisphere but with an increased fraction of myeloid cells, suggesting phagocytic uptake. Only 14% of liposome-positive cells were identified as tumor cells by human HLA-ABC staining. In contrast, co-HA and co-PLE NP+ cells exhibited significantly higher tumor cell enrichment compared to liposomes, comprising 25% and 42% of NP+ cells, respectively. Additionally, co-PLE NPs showed a significant decrease in the fraction of NP+ cells identified as astrocytes, oligodendrocytes, and unstained cells. Co-HA NPs showed a similarly decreased uptake by these cells, although to a lesser extent than PLE. The notable enrichment of tumor cells in the NP+ populations of co-LbL NPs and their reduced uptake by healthy glial cells indicate a potential for greater therapeutic impact and fewer off-target effects in therapeutic applications.

These findings suggest that while *in vitro* flow cytometry did not accurately predict the differential NP association across cell types, they were predictive of tumor cell affinity and specificity. We hypothesize that liposomes showed significant association with all cell types due to non-specific interactions between lipids and cell membranes, whereas LbL NPs exhibited tumor specificity through multivalent interactions with surface polymers. Although co-HA NPs showed higher tumor specificity than liposomes, the majority of the NP+ population were immune cells, possibly through interactions with the CD44, RHAMM, or scavenger receptors that are also highly expressed in these cells.[52] To focus more deeply on interactions of co-LbL NPs with myeloid cells and microglia, we visualized the NP uptake

using confocal microscopy. We used anti-Iba1 to identify both myeloid cells and microglia, and anti-human vimentin to identify human tumor cells, as these three cell types are responsible for the majority of NP uptake. Punctate co-HA NP fluorescence can be observed in Iba-1+ cells, suggesting phagocytosis as the primary mode of internalization (Figure 5G). In contrast, co-PLE NPs show a more uniform distribution without large NP aggregates (Figure 5H). This finding aligns with the flow cytometry experiments, where co-HA NPs exhibited higher NP-associated fluorescence in myeloid cells and microglia than co-PLE NPs, whereas co-PLE exhibited higher NP fluorescence in tumor cells than co-HA NPs and liposomes (Figure S13C). These results suggest that co-PLE NPs may be an effective delivery strategy for therapies that require tumor selectivity and broad distribution, whereas co-HA NPs may have therapeutic potential for more selectively targeting immune cells within the tumor environment. Notably, our data show that modulating surface chemistry using co-layered LbL NPs leads to distinct cellular fates after CED.

Conclusion

Taken together, our data demonstrate a method of applying LbL assembly to improve the distribution, retention, and cellular targeting of NPs for convection-enhanced delivery. By tuning the weight ratio of PEGylated and non-PEGylated outer layer polyanions, we investigated the therapeutic potential of two distinct LbL NPs featuring PLE and HA outer layers. We systematically determined the minimum incorporation of PEG to maintain colloidal stability in brain interstitial fluid while demonstrating high cellular uptake and cancer specificity *in vitro*. By incorporating an MRI contrast agent into the liposome core, we showed that LbL modification improves the distribution of NPs in healthy and glioblastoma tumor-bearing mice following CED. Gadolinium incorporation also enabled non-invasive monitoring of the distribution of NPs over time, showing prolonged retention with LbL systems compared to non-functionalized liposomes and low and high-molecular-weight chelates. While all NP exhibited a similar degree of overall cellular association, co-LbL NPs showed enhanced cancer cell uptake and specificity. Furthermore, we demonstrate that co-LbL assembly is a modular system where the outer layer identity and composition can be tuned to control the cellular fate *in vivo*. Future studies will focus on optimizing the NP concentration, dose, and injection parameters in the setting of therapeutic NPs. This approach offers insights into balancing the competing design criteria for locally delivered NPs targeting glioblastoma and may inform the development of tailored, targeted therapies.

Methods

Materials and Reagents

1,2-distearoyl-sn-glycero-3-phosphocholine (DSPC), 1,2-distearoyl-sn-glycero-3-phospho-(1’-rac-glycerol) (sodium salt) (DSPG), cholesterol, 1,2-distearoyl-sn-glycero-3-phosphoethanolamine (DSPE), 1,2-distearoyl-sn-glycero-3-phosphoethanolamine-N-diethylenetriaminepentaacetic acid (gadolinium salt) (PE-Gd), and 1-stearoyl-2-[(E)-4-(4-((4-butylphenyl)diazenyl)phenyl)butanoyl]-sn-glycero-3-phosphocholine (Azo-PC) were purchased from Avanti. BDP 650/665 with DBCO or NHS ester handles were purchased from Lumiprobe. Poly(L-arginine hydrochloride) (38 kDa), poly(L-glutamic

acid sodium salt) (15 kDa), and methoxy-poly(ethylene glycol)-block-poly(L-glutamic acid sodium salt) (PLE 15 kDa-b-PEG 5 kDa) were purchase from Alamanda Polymers. Sodium hyaluronate (20 kDa) was purchased from LifeCore Biomedical. Tangential flow filtration filters (D02-E100–05-N and C02-E100–05-N) were purchased from Repligen. For E21 and E57 glioma stem cell culture, DMEM/HAMS-F12, Accutase and 10% glucose were purchased from Millipore Sigma. 2-mercaptoethanol, MEM non-essential amino acids (100x), 7.5% sterile BSA solution, and B27 and N2 supplements were purchased from Thermo Fisher. Mouse EGF and human FGF were purchased from Peprotech. Cultrex Laminin was purchased from R&D systems. For BT145 cell culture, NeuroCult NS-A Human Proliferation Kit and 0.2% Heparin solution were purchased from STEMCELL. Human EGF and human FGF-2 were purchased from Miltenyi Biotec. Ultra-low attachment culture flasks and plates were purchased from Corning. For GBM22 culture, DMEM (#10–013-CV) was purchased from Corning. Primary human astrocytes (CAT #1800), brain vascular pericytes (CAT #1200), and brain microvascular endothelial cells (CAT #1000), and all media components were purchased from ScienCell. For HMC3 culture, Eagle's Minimum Essential Media (30–2003) was purchased from ATCC. Aggrewell plates and 37 μm reversible strainers were purchased from STEMCELL. Pierce methanol-free 16% formaldehyde was purchased from Thermo Fisher. Gadolinium and Terbium ICP standards were purchased from Inorganic Ventures. Gadolinium-labeled albumin was purchased from BioPAL. Gadavist (Gadobutrol 1 mmol/mL) was purchased from McKesson.

Cell Lines

E57 and E21 glioma stem cells were provided by the Pollard and Carragher Labs at the University of Edinburgh.[53] Cells were cultured in DMEM/HAMS-F12 supplemented with N2, B27, 10% glucose, 1% pen/strep, MEM non-essential amino acids, EGF (10 ng/mL) and FGF (10 ng/mL). Culture vessels were coated with Cultrex Laminin (R&D Systems) for 3 hours at 10 μg/mL before use. Laminin was added to cell culture media at a concentration of 2 μg/mL. Media was replaced twice weekly and passaged every 5–7 days at a ratio between 1:4 and 1:6 using Accutase (Sigma). BT145-luc neurospheres were provided by the Center for Patient Derived Models at the Dana Farber Cancer Institute. Neurospheres were cultured using the NeuroCult NS-A Human Proliferation Kit (STEMCELL), supplemented with hEGF (20 ng/mL), hFGF-2 (20 ng/mL), heparin (2 μg/mL). Cells were grown in ultra-low attachment flasks, and media was replaced twice per week. Neurospheres were dissociated using Accutase and mechanical trituration and split at a ratio of 1:6–1:8 every 7–9 days. GBM22 cells were provided by the Mayo Clinic Patient-Derived Xenograft National Resource and cultured in DMEM (Corning #10–013-CV) supplemented with 10% fetal bovine serum and 1% pen strep.[54] Media was replaced twice a week and passaged every 5–7 days at a ratio between 1:6 and 1:8 using 0.25% Trypsin-EDTA. HCM3 microglia were purchased from ATCC and cultured according to manufacturer instructions. Primary human astrocytes (CAT #1800), brain vascular pericytes (CAT #1200), and brain microvascular endothelial cells (CAT #1000) were all purchased from ScienCell and cultured according to manufacturer instructions. All experiments with primary cells were used within the number of population doublings guaranteed by the supplier. All cells were tested monthly for mycoplasma; the results were always negative.

NP Synthesis

To prepare fluorescently tagged lipids, 18:0 azidoethyl PC was mixed with 1.1 molar equivalents BDP 650/665 DBCO at 5 mg/mL lipid in chloroform. The solution was stirred overnight at room temperature, and the completion of the reaction was confirmed using thin-layer chromatography using a silica stationary phase and a mobile phase of 65:35:8 mixture of chloroform, methanol, and deionized water (MilliQ). The reaction was allowed to proceed until only a single fluorescence band was visible under a UV light.

Liposomes were prepared using a thin film hydration method. DSPC and cholesterol stocks were prepared in chloroform, and DSPG and DSPE were dissolved in a 1:1 mixture of chloroform and methanol. Cholesterol and lipids were combined in a round-bottom flask at a mole ratio of 31 Chol: 30.8 DSPC: 31 DSPG: 7 DSPE: 0.2 PC-BDP 650/665. To prepare gadolinium liposomes, cholesterol and lipids were combined at a mole ratio of 31 Chol: 30.8 DSPC: 31 DSPG: 5 PE-DTPA(Gd): 2 DSPE: 0.2 PC-BDP 650/665. The lipid solution was dried at room temperature using a BUCHI RotoVap system until completely dry (<50 mbar) and placed in a desiccator under vacuum overnight. The lipid film was rehydrated in a 25 mM HEPES 20 mM NaCl solution at a lipid concentration of 1 mg/mL and sonicated three times (1 minute on, 1 minute off) at 65 °C. Liposomes were extruded through nucleopore membranes until a Z-average diameter of 80–90 nm was obtained as measured by dynamic light scattering (Malvern Zetasizer Pro). Typically, this required passing through membranes twice with pore sizes of 200 nm, 100 nm, and 50 nm in consecutive stages. Traces of unconjugated dye were removed by tangential flow filtration (TFF).

To prepare LbL NPs, an equal volume of polyelectrolyte and NP solutions were mixed under brief sonication (3 seconds) and vortex mixed (3 seconds). Polyelectrolyte solutions were prepared in a buffer of 50 mM HEPES and 40 mM NaCl, except for HA which was prepared in 10 mM HEPES. NP solutions were prepared in deionized water (MilliQ) at 0.5 mg/mL lipids. The weight equivalent of polyelectrolyte to liposome core was 0.6x for poly-L-arginine (PLR) and 1.0 for poly-L-glutamine (PLE), hyaluronic acid (HA), and PEG-b-poly-L-glutamine (PLE-PEG). The same procedure was used for co-layering with PLE-PEG, except the polyelectrolyte solution contained a mixture of two polyelectrolytes (PLE and PLE-PEG, or HA and PLE-PEG), with a total weight equivalent of polyelectrolyte to liposome core of 1.0. After the adsorption of each layer, the excess polymer was removed using tangential flow filtration and concentrated between 0.5 mg/mL and 1 mg/mL.

Tangential Flow Filtration

NPs were purified using a Spectrum Labs KrosFlo II filtration system using Masterflex Teflon tubing. Hollow fiber filters D02-E100–05-N (batch volume >10 mL) and C02-E100–05-N (batch volume < 10 mL) with 100 kDa molecular weight cutoffs were used to purify excess polyelectrolytes from NP samples. Prior to purification, columns were washed with free polyelectrolyte solutions at 0.2 mg/mL for 5–10 minutes to saturate any nonspecific binding to the filters. For small batches, samples were concentrated to 2–3 mL by circulating NP solutions through the column without any permeate solution to make up for the lost volume exiting through the waste line. For purification, MilliQ water was connected to the permeate and samples were circulated for 5–10 buffer exchanges at a flow rate of 7 mL/min.

For large batches, samples were concentrated to 5 mL and purified at a flow rate of 40 mL/min. Columns were backflushed to recover any sample remaining in the column and tubing.

NP Characterization and Colloidal Stability

The hydrodynamic diameter, polydispersity, and zeta potential of the NPs were measured using dynamic light scattering (DLS) using a Malvern Zetasized Advanced Pro (λ= 633 nm). 25 μL NPs in DI water were mixed with 25 μL 50 mM HEPES 40 mM NaCl buffer, and subsequently diluted with 750 μL DI water and transferred to either polystyrene cuvettes, or DTS1070 folded capillary cuvettes for DLS analysis.

Artificial cerebrospinal fluid (aCSF) was prepared by dissolving the following concentrations of reagents into deionized water: 119 mM NaCl, 2.5 mM KCl, 1.3 mM $MgCl_2$, 2 mM $CaCl_2$, 1 mM NaH_2PO_4, 26.2 mM $NaHCO_3$, and 10 mM D-Glucose, all purchased from Millipore Sigma.[17] For colloidal stability studies, NPs were diluted to 0.01 mg/mL into either DI water or artificial cerebrospinal fluid (aCSF) supplemented with 0.02% sodium azide to prevent bacterial contamination. Solutions were incubated at 37 °C overnight, and the hydrodynamic diameter (z-average) and polydispersity index was measured with DLS.

NP uptake assay by Glioblastoma and Noncancerous cells

Glioblastoma and non-cancerous cells were seeded on 96-well plates at a density of 15,000 cells per well in 100 μL of the appropriate culture media and allowed to adhere overnight. Fluorescent normalized NP stocks were prepared in water at 0.1 mg/mL, and 5 μL was transferred to each well. Following an incubation period of 4 or 24 hours, cells were washed three times with PBS and detached with 25 μL of trypsin-EDTA or Accutase. 200 μL FACS buffer (PBS with 1% bovine serum albumin and 1 mM EDTA) with 1 μg/mL propidium iodide (Thermo Fisher) was used to quench the dissociation, and cells were pipetted vigorously to achieve a single-cell suspension. Cells were transferred to a new 96-well plate without any laminin or PLL coating, and samples were analyzed using a BD LSR II Flow Cytometer with a high-throughput sampler. Propidium-iodide staining was detected on the PE-Texas Red channel (ex. 488 em. 610/20), and BDP 650/665 tagged NPs were detected on the ACP channel (ex. 640 em. 670/30). Data were analyzed using FlowJo (version 10), and gates for single cells, live cells, and NP-positive cells were applied using untreated samples.

NP competition Binding Assay

We performed a cell receptor-blocking experiment using exogenous PLE or HA to evaluate the specific binding affinity of NPs to E57 cells. E57 cells were seeded on laminin-coated 96-well plates at a density of 15,000 cells per well in 100 μL of serum-free culture media and allowed to adhere overnight. Media was removed the next day and replaced with 90 μL of normal cell culture media, or media containing 100 μg/mL PLE (120 kDa) or HA (100 kDa) and incubated for 30 minutes at 37 °C. Fluorescent normalized NP stocks were prepared in water at 0.1 mg/mL, and 5 μL was transferred to each well. Following an incubation period of 2 hours, cells were washed three times with PBS, detached using 25 μL

Accutase, and resuspended in FACS buffer containing 1 μg/mL propidium iodide (Thermo Fisher). NP-associated fluorescence was analyzed using a BD LSR II Flow Cytometer, and the MFI values were normalized to the no-blocking conditions for each NP type.

Confocal Microscopy of Fixed NP-treated Cells

LabTek #1.5 borosilicate 8-well chamber slides were coated with 300 μL of rat tail collagen (Millipore Sigma) at a concentration of 50 μg/mL in 0.02N acetic acid for 5 minutes at room temperature. Chamber slides were washed once with PBS and air-dried for 5 minutes. 8,000 GBM22 cells were seeded per well in 300 μL media and allowed to adhere overnight before treatment with 5 μg/mL fluorescent NPs for 24 hours. Cells were carefully washed with HBSS on ice and incubated with 4 μg/mL wheat germ agglutinin-Alexa fluor 555 (Thermo Fisher) in ice-cold HBSS for 2 minutes. Cells were washed once with ice-cold PBS without incubation to remove excess wheat germ agglutinin and subsequently washed with PBS twice for 5 minutes before fixation with 4% paraformaldehyde (Pierce) for 15 minutes at room temperature. The cells were washed three more times with PBS and incubated with 4 μM Hoechst 33432 (Thermo Fisher) for 5 minutes at room temperature. Cells were imaged using an Olympus FV1200 confocal microscope with a 100x oil immersion objective. Images were pseudocoloured using FIJI.

NP Uptake and Penetration Assay by Glioblastoma Spheroids

To analyze spheroid penetration by flow cytometry, 5000 BT145-luc cells per well were seeded in 96-well spheroid microplates (Corning) and centrifuged at 200 × g for 3 minutes. The spheroids were monitored for 3 days until a single spheroid was present in each well, with a diameter of approximately 300 μm. 5 μg/mL NPs were added to each well and spheres were incubated for 4 or 24 hours. The spheroids were washed with PBS and treated with 50 μL of Accutase at room temperature for 5 minutes, followed by vigorous mixing with a pipette to obtain a single-cell suspension. The suspension was centrifuged at 300 × g for 3 minutes and resuspended in FACS buffer (PBS containing 1% BSA and 1 mM EDTA) along with 1 μg/mL propidium iodide for flow cytometric analysis. The data were analyzed using FlowJo version 10.

To analyze spheroid penetration by confocal microscopy, BT145-luc spheroids were prepared by adding 1.5 * 10^6 cells per well in AggreWell 800 24-well plates (STEMCELL) following manufacturer instructions and incubated for 48 hours. Spheroids were dislodged with a pipette and filtered through a 70 μm reversible strainer (STEMCELL). Approximately 100 spheroids per well were plated in 24-well plates in 1 mL media and incubated with 5 μg/mL fluorescent NPs for 24 hours. Following incubation, spheroids were filtered through a 70 μm reversible strainer and washed with 2–3 mL PBS. The spheroids were transferred to 15 mL tubes and allowed to settle and washed with PBS twice. Spheroids were suspended in a 30% (w/w) sucrose solution and incubated at 4 °C overnight with gentle agitation. The spheroids were washed twice with PBS, resuspended in 200 μL of Tissue-TEK optimal cutting temperature compound, transferred to a 15 × 15 mm tissue mold, and allowed to settle before being frozen on dry ice. 10 μm sections were cut using a cryostat. Before confocal microscopy, slides were dried at room temperature for 30 minutes, resuspended in PBS containing 10 μM Hoechst 33432 and coverslipped using prolonged gold antifade

reagent (Thermo Fisher). Spheroid sections were imaged using a Leica SP8 confocal microscope with a 25x water immersion objective. The sections containing the midline of the spheroid were used for analysis and were identified by comparing the diameters of the spheroid sections on each slide. Data were analyzed using FIJI using the Radial Plot Profile plugin. Data from three spheroids per treatment were averaged, and radial distances were normalized to account for slight differences in spheroid diameter.

Gadolinium-NP characterization

The gadolinium content of liposomes containing 5 mol % PE-DTPA(Gd) was measured using inductively coupled plasma mass spectroscopy (Agilent 7900). NPs were diluted to 0.1 mg/mL in 2% nitric acid containing 10 ppb terbium as an internal standard. A 10-point standard curve was prepared by serial dilution of a 10 ppm solution of gadolinium ICP standard (Inorganic ventures).

Animal Studies

All animal experiments were approved by the Massachusetts Institute of Technology Committee on Animal Care (CAC, protocol number 2207000386) and were conducted under the oversight of the Division of Comparative Medicine (DCM). NCR/Nude mice were purchased from Taconic and housed in cages with a maximum of five animals per cage, under controlled temperature (25 °C), 12-hour light-dark cycles, and provided with free access to food and water. Both male and female mice were used for all experiments, and the mice were 7–10 weeks at the time of the experiment. Group sizes were determined using MANOVA for repeated measures (alpha = 0.05, power = 0.95) based on effect sizes and standard deviations from pilot experiments.

CED in Healthy Mice

Mice were anesthetized with a mixture of ketamine (100 mg/kg) and xylazine (10 mg/kg) administered intraperitoneally. Mice were transferred to a 37 °C heating pad, and ophthalmic ointment was applied using a sterile Q-tip. Anesthesia was confirmed using a toe pinch, and Buprenorphine SR (1 mg/mL) was administered subcutaneously. The skull was swabbed with alternating Betadine and 70% ethanol three times, and a midline skin incision approximately 1 cm in length was made using a sterile scalpel. The periosteum was swabbed with a sterile Q-tip to expose the bregma, and a lidocaine 2.5%/prilocaine 2.5% cream was applied to the ears before placement on a stereotaxic frame (Stoelting). A small burr hole located 1.8 mm right and 0.8 mm anterior to the bregma was drilled using a 1 mm steel drill bit. Approximately 6 μL NP or control solution was drawn into a 10 μL Hamilton syringe fitted with a custom-made 34 G stainless steel needle protruding 1 mm from a 27 G blunt-tipped needle. The Stereodrive software was used to align the needle with the burr hole and lower it to a depth of 3.5 mm from the skull surface. The needle was left for 2 minutes to equilibrate in the brain prior to infusion of either a 5% dextrose control, Gadavist, Galbumin, or NPs at a normalized gadolinium concentration of 0.0375 mM. The carrier fluid for all samples was 5% dextrose in sterile water. A motorized injection robot (Stoelting) was used to infuse at a ramped injection protocol: 1 μL at 0.2 μL/min, 2 μL at 0.5 μL/min, and 2 μL at 0.8 μL/min. After an additional 2 minutes of equilibration, the needle was raised at a rate of 1 mm/min. The incision was closed using 5–0 monocryl sutures (Ethicon) and sealed

with tissue glue. Animals were placed in a heated cage for post-op recovery and monitored daily for the first 4 days, then twice weekly until the experimental endpoint was reached.

Magnetic Resonance Imaging

Magnetic Resonance Imaging (MRI) was performed *in vivo* on a 7T MRI operated by Bruker AV4 NeoBioSpec70–20USR console, equipped with a 114mm 660mT/m actively shielded gradient and a QSN075/040 RF coil (Bruker BioSpin, Rheinstetten, Germany). Mice were anesthetized by inhalation of 2.5% isofluorane and maintained on 2–2.5% isofluorane throughout data collection. Body temperature and respiration rate were monitored by SAII monitoring and gating system (Small Animal Instruments Inc., Stony Brook). Anatomical brain images were collected and reconstructed within Bruker Paravision PV360 v2.0. T2 Weighted images were obtained using the TurboRARE protocol with TR/TE=3000/25 ms, number of averages=4, and RARE factor of 8. T1 weighted images were acquired with T1_FLASH at TR/TE=360/4.5 ms and a flip angle of 70°. Both axial and coronal datasets were obtained with the geometric parameters of 256×256 matrix, field of view (FOV)=20×20mm^2, interleaved number of slices=20, no gap and slice thickness=0.5mm. Images were converted to DICOM format and exported to 3D slicer for analysis. The 3D volume of nanoparticle distribution (V_D) was calculated from the axial datasets by applying a 20% intensity threshold to the average T1-weighted signal of the untreated hemisphere.

For relaxation measurements, T1-mapping of NP samples at 0.5, 1, 2, and 3 mg/mL lipids was executed using a RARE sequence (T1map_RARE) with one Echo image, Rare Factor of 2, Echo Spacing of 8.5ms, and 6 T1 experiments with TRs of 5500ms, 3000ms, 1500ms, 800ms, 400ms and 200ms respectively. T1 relaxation time was calculated within Paravision using the fitting model below:

$$Y = A + C \times \left(1 - exp\left(\frac{-t}{T1}\right)\right)$$

where A is the absolute bias, and C is signal intensity.

Orthotopic Tumor Inoculation

BT145-Luc spheroids grown in culture for 2–3 weeks were dissociated into single cells using Accutase and suspended in sterile PBS. 100,000 cells in 3 μL were administered intracranially over 3 minutes using the same procedure and coordinate as CED. Bone wax was used to fill the burr hole to prevent tumor cells from leaking into the extracranial space. Tumor growth was monitored weekly over 100–120 days by measuring cranial bioluminescence using IVIS (Perkin Elmer). Animal weight was recorded each week. At select time points, the tumor volumes of mice with the highest luminescence were estimated using T2 MRI.

CED in Tumor-Bearing Mice

CED was performed on tumor-bearing mice once bioluminescence growth reached the log phase (corresponding to an average radiance of approximately 10,000 [p/s/cm^2/sr]), and

tumors were visible on T2 MRI. Mice were stratified into treatment groups based on the exact bioluminescence signal recorded from IVIS. To account for potential experimental variability across different days, each day of CED treatments included a mixture of different treatment groups. CED was performed using the same protocol for healthy mice by re-opening the burr hole used for tumor inoculation. T1 anatomical MRI images were obtained 24 hours after CED, and the mice were sacrificed for either histology or flow cytometry.

Frozen Histology and Immunofluorescence

For immunofluorescence studies, brains were removed and fixed in 10% formalin overnight at room temperature. The olfactory bulb and cerebellum were removed, and the remaining brain tissue was fixed in fresh 10% formalin for an additional hour. Tissues were cryoprotected in 15% (w/w) sucrose in PBS overnight, followed by 30% (w/w) sucrose in PBS for an additional 24 hours. Brains were embedded in optimal cutting temperature compound (TissueTek), placed in a 15 mm × 15 mm tissue mold, and frozen on dry ice. Frozen tissue was stored at −80 °C prior to sectioning. Serial sections with a thickness of 10 μm were cut using a cryostat (Leica), sequentially adding one section to a slide, with 10 slides total. This process was repeated 6 times, resulting in 10 slides, each with six brain sections spaced 100 μm apart. A total of three or four sets of 10 slides were collected for each brain, to cover the entire region of NP distribution.

For visualization of NP distribution and cell nuclei alone, slides with frozen sections were dried at room temperature for 30 minutes in the dark and rehydrated in PBS for 10 minutes. Slides were stained with Hoechst 33432 (10 μM, Thermo Fisher) in PBS for 10 minutes. Sections were washed three times for 5 minutes each in PBS and mounted with ProLong Gold Antifade Mounting Medium. For immunofluorescence, slides were dried at room temperature for 30 minutes, rehydrated in PBS for 10 minutes, and permeabilized with 0.2% triton-X in PBS (Millipore Sigma) for 15 minutes. Slides were washed three times for 5 minutes each in PBS and blocked using 10% normal goat serum (Cell Signalling Technologies) and 0.1% (w/w) Tween-20 (Millipore Sigma) in PBS. Primary antibodies were diluted in PBS with 1% (w/w) bovine serum albumin and 0.1% (w/w) Tween 20 at the following dilutions: vimentin-AF488 (Abcam ab195877) 1:300, ALDH1L1 (Abcam ab307696) 1:500, NeuN (Abcam ab177487) 1:500, Iba1 (Abcam ab178846) 1:500. Slides were incubated with the primary antibodies overnight at 4 °C, then washed three times with PBS for 5 minutes each. The anti-rabbit AF488-plus secondary antibody (Invitrogen A32731) was diluted 1:1000 in PBS with 1% BSA and added to the slides for a 1-hour incubation at room temperature. Slides were washed three times with PBS for 5 minutes each and stained with DAPI (5 μg/mL, Thermo Fisher) in PBS for 10 minutes. Sections were washed three times for 5 minutes each in PBS and mounted with ProLong Gold Antifade Mounting Medium. Slides were imaged using confocal microscopy (Leica SP8) and pseudocoloured using FIJI.

Toxicity Study

Brains from healthy mice from each treatment group were processed for histology to evaluate short-term (3 days) and long-term (3 weeks) toxicity. Brains were removed and fixed in 10% formalin overnight at room temperature, and a coronal cut was made using a

razor blade to expose two surfaces at the injection site. The tissue was fixed in fresh 10% formalin for an additional hour and placed cut-side up in a tissue cassette. The tissue was embedded in paraffin, and then 5 pairs of two 4 μm sections were taken at intervals of 50 μm. As a result, the total depth of the examined or viewed tissue was 500 μm. Slides were stained with H&E, and a certified pathologist blindly evaluated the tissue sections.

Flow Cytometry of CED-Treated Mouse Brains

24 hours after NP CED, mice were euthanized, and brains were collected and placed in cold D-PBS on ice. The olfactory bulb and cerebellum were removed, and a sagittal cut was made to divide the brain into two hemispheres; the right hemisphere received the NP injection, while the left hemisphere was used as control tissue with no NP injection. A single-cell suspension from each hemisphere was obtained using the Miltenyi Adult Brain Dissociation Kit, following manufacturer instructions. Briefly, tissue was cut into 6–8 smaller pieces and placed in a gentleMACS C-tube with the kit-supplied enzymes. Mechanical dissociation was carried out on a GenlteMACS octo dissociator, with the tissue placed in a 37 °C orbital shaker for the incubation steps. Dissociated tissue was filtered through a 70 μm strainer, centrifuged, and resuspended in debris removal solution with an overlay of D-PBS. Contrary to manufacturer instructions, 50% centrifuge acceleration and no break were applied to achieve optimal separation of three layers: supernatant, debris, and cell suspension. The cell suspension was collected, centrifuged again, and resuspended in red blood cell lysis solution. A small aliquot of the resuspended cells was mixed with an equal volume of 0.4% Trypan blue solution, and live cells were counted. Cells were resuspended at a concentration of 10^6 cells in 90 μL in FACS staining buffer (PBS with 0.5% BSA and 2 mM EDTA) containing a 1:100 dilution of Zombie Aqua Viability Dye (Thermo Fisher). Cells were incubated for 10 minutes in the dark at 4 °C, and 10 μL of mouse FcR blocking reagent (Miltenyi Biotec) was added to each tube. Tubes were mixed by pipetting and cells were incubated for additional 10 minutes at 4 °C. Primary antibodies were then added at a 1:50 dilution and incubated for 10 minutes at 4 °C: CD45-BUV395 (BD 565967), CD11b-BV480 (Miltenyi 130–113-810), HLA-ABC-VioBright515 (Miltenyi 130–126-902), O4-PE (Miltenyi 130–117-711), ACSA-2-PE-Vio615 (Miltenyi 130–116-249), CD31-PE-Vio770 (Miltenyi 130–111-542), CD140b-APC-Vio770 (Miltenyi 130–118-469). Cells were washed by adding 1.5 mL FACS buffer and centrifuged at 300 × g for 10 minutes. Cells were resuspended in 0.5 mL FACS buffer and transferred to flow cytometry tubes.

Flow cytometry was performed using FACSymphony A3 Cell Analyzer (BD) equipt with FACSDiva software, with post-collection data analysis performed in FlowJo version 10. During data collection, single cells were selected using FSC and SSC gates, and laser intensities were set using single-stain controls derived from the same cell population for each fluorophore used. Fluorescence compensation was performed using the auto-compensation tool within FACSDiva software each time the experiment was run. After gating single cells, dead cells were excluded based on Zombie Aqua Viability Dye fluorescence, and individual cell populations were gated using fluorescence associated with each surface marker (refer to Figure S13 for a detailed gating strategy). Gates were set using fluorescence-minus-one controls each time the experiment was run. A stopping gate of 30,000 cells was applied to the single, live cell population, and the percentage of each

cell type relative to this population was used to derive the overall cellular distribution. To derive the cellular distribution of NP+ cells, an NP-fluorescence gate was first set using a left-hemisphere sample that did not receive a NP injection, and the same cell-type gating strategy was applied to the NP+ fraction. The left-hemisphere sample was also used to set gates for the percentage of each cell type that was NP-positive.

Statistical Analysis

All statistical analysis was performed using GraphPad Prism 9. Information on statistical tests is provided in the associated figure caption. Unless otherwise noted, single comparisons among normally distributed data were made using a two-sided Student's T-test, and multiple comparisons were made using ANOVA with Tukey's post hoc correction.

Supplementary Material

Refer to Web version on PubMed Central for supplementary material.

Acknowledgments

The authors would like to thank the Koch Institute's Robert A. Swanson (1969) Biotechnology Center for technical support, specifically the Preclinical Modeling, Imaging and Testing Core, Flow Cytometry Core, and Microscopy Core. This work was supported in part by the Koch Institute Support (core) Grant P30-CA14051 from the National Cancer Institute and by the Bridge Project, a partnership between the Koch Institute for Integrative Cancer Research at MIT and the Dana-Farber/Harvard Cancer Center. We would also like to acknowledge funding from Cancer Research UK and the Brain Tumor Charity grant REF: C42454/A28596. Glioma stem cell models E57 and E21 were made available through the Glioma Cellular Genetics Resource funded by Cancer Research UK. A.J.P. is supported by the Natural Sciences and Engineering Research Council of Canada (NSERC) [CGSD3 – 557538 - 2021]. N.G.L. was supported by a postdoctoral fellowship from the Ludwig Center at MIT's Koch Institute for Integrative Cancer Research. J.P.S. is supported by the Charles W. (1955) and Jennifer C. Johnson Cancer Research Fund, Cannonball Kids' Cancer Foundation, the Rally Foundation for Childhood Cancer Research and a 2022 AACR-Day One Biopharmaceuticals Pediatric Cancer Research Fellowship. We would like to thank Alice Li for her assistance in interpreting H&E histology. The schematic in Figure 5 was created using BioRender.com. Finally, we would like to thank Elad Deiss-Yehiely for his thoughtful review of this manuscript.

P.T.H. is a co-founder and member of the board of LayerBio, a member of the Scientific Advisory Board of Moderna, and a member of the Board of Alector, Advanced Chemotherapy Technologies, and Burroughs-Wellcome Fund. All other authors report no competing interests.

Data Availability

The data for this study are available within the article, with additional data available in the supporting information. Additional raw data are available upon reasonable request from the corresponding author.

References

(1). Weller M; Wick W; Aldape K; Brada M; Berger M; Pfister SM; Nishikawa R; Rosenthal M; Wen PY; Stupp R; Reifenberger G Glioma. Nat. Rev. Dis. Primer 2015, 1.

(2). Zanders ED; Svensson F; Bailey DS Therapy for Glioblastoma: Is It Working? Drug Discov. Today 2019, 24, 1193–1201. [PubMed: 30878561]

(3). De Bonis P; Anile C; Pompucci A; Fiorentino A; Balducci M; Chiesa S; Lauriola L; Maira G; Mangiola A The Influence of Surgery on Recurrence Pattern of Glioblastoma. Clin. Neurol. Neurosurg. 2013, 115, 37–43. [PubMed: 22537870]

(4). Harder BG; Blomquist MR; Wang J; Kim AJ; Woodworth GF; Winkles JA; Loftus JC; Tran NL Developments in Blood-Brain Barrier Penetrance and Drug Repurposing for Improved Treatment of Glioblastoma. Front. Oncol. 2018, 8. [PubMed: 29450192]

(5). Komotar RJ; Otten ML; Moise G; Connolly ES Radiotherapy plus Concomitant and Adjuvant Temozolomide for Glioblastoma—A Critical Review. Clin. Med. Oncol. 2008, 2, 421–422. [PubMed: 21892310]

(6). Bobo RH; Laske DW; Akbasak A; Morrison PF; Dedrick RL; Oldfield EH Convection-Enhanced Delivery of Macromolecules in the Brain. Proc. Natl. Acad. Sci. 1994, 91, 2076–2080. [PubMed: 8134351]

(7). Sampson JH; Singh Achrol A.; Aghi MK.; Bankiewicz K.; Bexon M.; Brem S; Brenner A.; Chandhasin C.; Chowdhary S.; Coello M.; Ellingson BM.; Floyd JR.; Han S.; Kesari S.; Mardor Y.; Merchant F.; Merchant N.; Randazzo D.; Vogelbaum M.; Vrionis F.; Wembacher-Schroeder.; Zabek M.; Butowski N. Targeting the IL4 Receptor with MDNA55 in Patients with Recurrent Glioblastoma: Results of a Phase IIb Trial. Neuro-Oncol. 2023, noac285.

(8). Souweidane MM; Kramer K; Pandit-Taskar N; Zhou Z; Haque S; Zanzonico P; Carrasquillo JA; Lyashchenko SK; Thakur SB; Donzelli M; Turner RS; Lewis JS; Cheung N-KV; Larson SM; Dunkel IJ Convection-Enhanced Delivery for Diffuse Intrinsic Pontine Glioma: A Single-Centre, Dose-Escalation, Phase 1 Trial. Lancet Oncol. 2018, 19, 1040–1050. [PubMed: 29914796]

(9). Jahangiri A; Chin AT; Flanigan PM; Chen R; Bankiewicz K; Aghi MK Convection-Enhanced Delivery in Glioblastoma: A Review of Preclinical and Clinical Studies. J. Neurosurg. 2017, 126, 191–200. [PubMed: 27035164]

(10). Lidar Z; Mardor Y; Jonas T; Pfeffer R; Faibel M; Nass D; Hadani M; Ram Z Convection-Enhanced Delivery of Paclitaxel for the Treatment of Recurrent Malignant Glioma: A Phase I/II Clinical Study. J. Neurosurg. 2004, 100, 472–479. [PubMed: 15035283]

(11). Bruce JN; Fine RL; Canoll P; Yun J; Kennedy BC; Rosenfeld SS; Sands SA; Surapaneni K; Lai R; Yanes CL; Bagiella E; DeLaPaz RL Regression of Recurrent Malignant Gliomas With Convection-Enhanced Delivery of Topotecan. Neurosurgery 2011, 69, 1272–1280. [PubMed: 21562434]

(12). Saito R; Kanamori M; Sonoda Y; Yamashita Y; Nagamatsu K; Murata T; Mugikura S; Kumabe T; Wembacher-Schröder E; Thomson R; Tominaga T Phase I Trial of Convection-Enhanced Delivery of Nimustine Hydrochloride (ACNU) for Brainstem Recurrent Glioma. Neuro-Oncol. Adv. 2020, 2, 1–9.

(13). Ji T; Kohane DS Nanoscale Systems for Local Drug Delivery. Nano Today 2019, 28, 100765. [PubMed: 32831899]

(14). Reddy LH Drug Delivery to Tumours: Recent Strategies. J. Pharm. Pharmacol. 2010, 57, 1231–1242.

(15). Hobbs SK; Monsky WL; Yuan F; Roberts WG; Griffith L; Torchilin VP; Jain RK Regulation of Transport Pathways in Tumor Vessels: Role of Tumor Type and Microenvironment. Proc. Natl. Acad. Sci. 1998, 95, 4607–4612. [PubMed: 9539785]

(16). Nance EA; Woodworth GF; Sailor KA; Shih T-Y; Xu Q; Swaminathan G; Xiang D; Eberhart C; Hanes J A Dense Poly(Ethylene Glycol) Coating Improves Penetration of Large Polymeric Nanoparticles Within Brain Tissue. Sci. Transl. Med. 2012, 4.

(17). Curtis C; Toghani D; Wong B; Nance E Colloidal Stability as a Determinant of Nanoparticle Behavior in the Brain. Colloids Surf. B Biointerfaces 2018, 170, 673–682. [PubMed: 29986264]

(18). Schneider CS; Perez JG; Cheng E; Zhang C; Mastorakos P; Hanes J; Winkles JA; Woodworth GF; Kim AJ Minimizing the Non-Specific Binding of Nanoparticles to the Brain Enables Active Targeting of Fn14-Positive Glioblastoma Cells. Biomaterials 2015, 42, 42–51. [PubMed: 25542792]

(19). Nance E; Zhang C; Shih TY; Xu Q; Schuster BS; Hanes J Brain-Penetrating Nanoparticles Improve Paclitaxel Efficacy in Malignant Glioma Following Local Administration. ACS Nano 2014, 8, 10655–10664. [PubMed: 25259648]

(20). Song E; Gaudin A; King AR; Seo Y-E; Suh H-W; Deng Y; Cui J; Tietjen GT; Huttner A; Saltzman WM Surface Chemistry Governs Cellular Tropism of Nanoparticles in the Brain. Nat. Commun. 2017, 8, 15322. [PubMed: 28524852]

(21). Pozzi D; Colapicchioni V; Caracciolo G; Piovesana S; Laura Capriotti A.; Palchetti S.; Grossi SD.; Riccioli A.; Amenitsch H.; Laganà A. Effect of Polyethyleneglycol (PEG) Chain Length on the Bio–Nano-Interactions between PEGylated Lipid Nanoparticles and Biological Fluids: From Nanostructure to Uptake in Cancer Cells. Nanoscale 2014, 6, 2782–2792. [PubMed: 24463404]

(22). Lam FC; Morton SW; Wyckoff J; Vu Han TL; Hwang MK; Maffa A; Balkanska-Sinclair E; Yaffe MB; Floyd SR; Hammond PT Enhanced Efficacy of Combined Temozolomide and Bromodomain Inhibitor Therapy for Gliomas Using Targeted Nanoparticles. Nat. Commun. 2018, 9.

(23). Kaluzova M; Bouras A; Machaidze R; Hadjipanayis CG Targeted Therapy of Glioblastoma Stem-like Cells and Tumor Non-Stem Cells Using Cetuximab-Conjugated Iron-Oxide Nanoparticles. Oncotarget 2015, 6, 8788–8806. [PubMed: 25871395]

(24). van Solinge TS; Nieland L; Chiocca EA; Broekman MLD D. Advances in Local Therapy for Glioblastoma — Taking the Fight to the Tumour. Nat. Rev. Neurol. 2022, 0123456789.

(25). Poon Z; Lee JB; Morton SW; Hammond PT Controlling in Vivo Stability and Biodistribution in Electrostatically Assembled Nanoparticles for Systemic Delivery. Nano Lett. 2011, 11, 2096–2103. [PubMed: 21524115]

(26). Morton SW; Poon Z; Hammond PT The Architecture and Biological Performance of Drug-Loaded LbL Nanoparticles. Biomaterials 2013, 34, 5328–5335. [PubMed: 23618629]

(27). Dang X; Gu L; Qi J; Correa S; Zhang G; Belcher AM; Hammond PT Layer-by-Layer Assembled Fluorescent Probes in the Second near-Infrared Window for Systemic Delivery and Detection of Ovarian Cancer. Proc. Natl. Acad. Sci. 2016, 113, 5179–5184. [PubMed: 27114520]

(28). Straehla JP; Hajal C; Safford HC; Offeddu GS; Boehnke N; Dacoba TG; Wyckoff J; Kamm RD; Hammond PT A Predictive Microfluidic Model of Human Glioblastoma to Assess Trafficking of Blood–Brain Barrier-Penetrant Nanoparticles. Proc. Natl. Acad. Sci. 2022, 119, e2118697119. [PubMed: 35648828]

(29). Butowski N A Phase I Study of Convection-Enhanced Delivery of Liposomal-Irinotecan Using Real-Time Imaging With Gadolinium In Patients With Recurrent High Grade Glioma; Clinical trial registration NCT02022644; clinicaltrials.gov, 2022. https://clinicaltrials.gov/ct2/show/NCT02022644 (accessed 2023-04-30).

(30). Correa S; Boehnke N; Barberio AE; Deiss-Yehiely E; Shi A; Oberlton B; Smith SG; Zervantonakis I; Dreaden EC; Hammond PT Tuning Nanoparticle Interactions with Ovarian Cancer through Layer-by-Layer Modification of Surface Chemistry. ACS Nano 2020, 14, 2224–2237. [PubMed: 31971772]

(31). Boehnke N; Straehla JP; Safford HC; Kocak M; Rees MG; Ronan M; Rosenberg D; Adelmann CH; Chivukula RR; Nabar N; Berger AG; Lamson NG; Cheah JH; Li H; Roth JA; Koehler AN; Hammond PT Massively Parallel Pooled Screening Reveals Genomic Determinants of Nanoparticle Delivery. Science 2022, 377 (6604).

(32). Deiss-Yehiely E; Brucks SD; Boehnke N; Pickering AJ; Kiessling LL; Hammond PT Surface Presentation of Hyaluronic Acid Modulates Nanoparticle-Cell Association. Bioconjug. Chem. 2022.

(33). Mooney KL; Choy W; Sidhu S; Pelargos P; Bui TT; Voth B; Barnette N; Yang I The Role of CD44 in Glioblastoma Multiforme. J. Clin. Neurosci. 2016, 34, 1–5. [PubMed: 27578526]

(34). Correa S; Boehnke N; Deiss-Yehiely E; Hammond PT Solution Conditions Tune and Optimize Loading of Therapeutic Polyelectrolytes into Layer-by-Layer Functionalized Liposomes. ACS Nano 2019, 13, 5623–5634. [PubMed: 30986034]

(35). Cowman MK; Spagnoli C; Kudasheva D; Li M; Dyal A; Kanai S; Balazs EA Extended, Relaxed, and Condensed Conformations of Hyaluronan Observed by Atomic Force Microscopy. Biophys. J. 2005, 88, 590–602. [PubMed: 15489305]

(36). Pibuel MA; Poodts D; Díaz M; Hajos SE; Lompardía SL The Scrambled Story between Hyaluronan and Glioblastoma. J. Biol. Chem. 2021, 296, 100549. [PubMed: 33744285]

(37). Barberio AE; Smith SG; Correa S; Nguyen C; Nhan B; Melo M; Tokatlian T; Suh H; Irvine DJ; Hammond PT Cancer Cell Coating Nanoparticles for Optimal Tumor-Specific Cytokine Delivery. ACS Nano 2020, 14, 11238–11253. [PubMed: 32692155]

(38). Mulder WJM; Strijkers GJ; Griffioen AW; Van Bloois L; Molema G; Storm G; Koning GA; Nicolay K A Liposomal System for Contrast-Enhanced Magnetic Resonance Imaging of Molecular Targets. Bioconjug. Chem. 2004, 15, 799–806. [PubMed: 15264867]

(39). Šimečková P; Hubatka F; Kotouček J; Turánek Knötigová P; Mašek J; Slavík J; Kováč O; Neča J; Kulich P; Hrebík D; Stráská J; Pěnčíková K; Procházková J; Diviš P; Macaulay S; Mikulík R; Raška M; Machala M; Turánek J Gadolinium Labelled Nanoliposomes as the Platform for MRI Theranostics: In Vitro Safety Study in Liver Cells and Macrophages. Sci. Rep. 2020, 10, 1–13. [PubMed: 31913322]

(40). Singh R; Bellat V; Wang M; Schweitzer ME; Wu YL; Tung CH; Souweidane MM; Law B Volume of Distribution and Clearance of Peptide-Based Nanofiber after Convection-Enhanced Delivery. J. Neurosurg. 2018, 129, 10–18.

(41). Nordling-David MM; Yaffe R; Guez D; Meirow H; Last D; Grad E; Salomon S; Sharabi S; Levi-Kalisman Y; Golomb G; Mardor Y Liposomal Temozolomide Drug Delivery Using Convection Enhanced Delivery. J. Controlled Release 2017, 261, 138–146.

(42). Grahn AY; Bankiewicz KS; Dugich-Djordjevic M; Bringas JR; Hadaczek P; Johnson GA; Eastman S; Luz M Non-PEGylated Liposomes for Convection-Enhanced Delivery of Topotecan and Gadodiamide in Malignant Glioma: Initial Experience. J. Neurooncol. 2009, 95, 185–197. [PubMed: 19466380]

(43). Drummond DC; Noble CO; Guo Z; Hong K; Park JW; Kirpotin DB Development of a Highly Active Nanoliposomal Irinotecan Using a Novel Intraliposomal Stabilization Strategy. Cancer Res. 2006, 66, 3271–3277. [PubMed: 16540680]

(44). Fugit KD; Xiang T-X; Choi DH; Kangarlou S; Csuhai E; Bummer PM; Anderson BD Mechanistic Model and Analysis of Doxorubicin Release from Liposomal Formulations. J. Controlled Release 2015, 217, 82–91.

(45). Zhang C; Mastorakos P; Sobral M; Berry S; Song E; Nance E; Eberhart CG; Hanes J; Suk JS Strategies to Enhance the Distribution of Nanotherapeutics in the Brain. J. Controlled Release 2017, 267, 232–239.

(46). Krauze MT; Noble CO; Kawaguchi T; Drummond D; Kirpotin DB; Yamashita Y; Kullberg E; Forsayeth J; Park JW; Bankiewicz KS Convection-Enhanced Delivery of Nanoliposomal CPT-11 (Irinotecan) and PEGylated Liposomal Doxorubicin (Doxil) in Rodent Intracranial Brain Tumor Xenografts. Neuro-Oncol. 2007, 9, 393–403. [PubMed: 17652269]

(47). Barberio AE; Smith SG; Pires IS; Iyer S; Reinhardt F; Melo MB; Suh H; Weinberg RA; Irvine DJ; Hammond PT Layer-by-Layer Interleukin-12 Nanoparticles Drive a Safe and Effective Response in Ovarian Tumors. Bioeng. Transl. Med. 2023, 8, e10453. [PubMed: 36925719]

(48). van Solinge TS; Nieland L; Chiocca EA; Broekman MLD. Advances in Local Therapy for Glioblastoma — Taking the Fight to the Tumour. Nat. Rev. Neurol. 2022, 0123456789.

(49). Green AL; Ramkissoon SH; McCauley D; Jones K; Perry JA; Hsu JH-R; Ramkissoon LA; Maire CL; Hubbell-Engler B; Knoff DS; Shacham S; Ligon KL; Kung AL Preclinical Antitumor Efficacy of Selective Exportin 1 Inhibitors in Glioblastoma. Neuro-Oncol. 2015, 17, 697–707. [PubMed: 25366336]

(50). Anyaegbu CC; Mao Y; McGonigle T; Raja S; Clarke T; Black AMB; Solomon T; Fuller K; Fitzgerald M Simultaneous Flow Cytometric Characterization of Multiple Cell Types and Metabolic States in the Rat Brain after Repeated Mild Traumatic Brain Injury. J. Neurosci. Methods 2021, 359, 109223. [PubMed: 34004202]

(51). Schroeter CB; Herrmann AM; Bock S; Vogelsang A; Eichler S; Albrecht P; Meuth SG; Ruck T Article One Brain—All Cells: A Comprehensive Protocol to Isolate All Principal Cns-Resident Cell Types from Brain and Spinal Cord of Adult Healthy and Eae Mice. Cells 2021, 10, 1–25.

(52). Sawada R; Nakano-Doi A; Matsuyama T; Nakagomi N; Takayuki Nakagomi T CD44 Expression in Stem Cells and Niche Microglia/Macrophages Following Ischemic Stroke. Stem Cell Investig. 2020, 7, 4–4.

(53). Pollard SM; Yoshikawa K; Clarke ID; Danovi D; Stricker S; Russell R; Bayani J; Head R; Lee M; Bernstein M; Squire JA; Smith A; Dirks P Glioma Stem Cell Lines Expanded in Adherent Culture Have Tumor-Specific Phenotypes and Are Suitable for Chemical and Genetic Screens. Cell Stem Cell 2009, 4, 568–580. [PubMed: 19497285]

(54). Carlson BL; Pokorny JL; Schroeder MA; Sarkaria JN Establishment, Maintenance, and In Vitro and In Vivo Applications of Primary Human Glioblastoma Multiforme (GBM) Xenograft Models for Translational Biology Studies and Drug Discovery. Curr. Protoc. Pharmacol. 2011, 52.

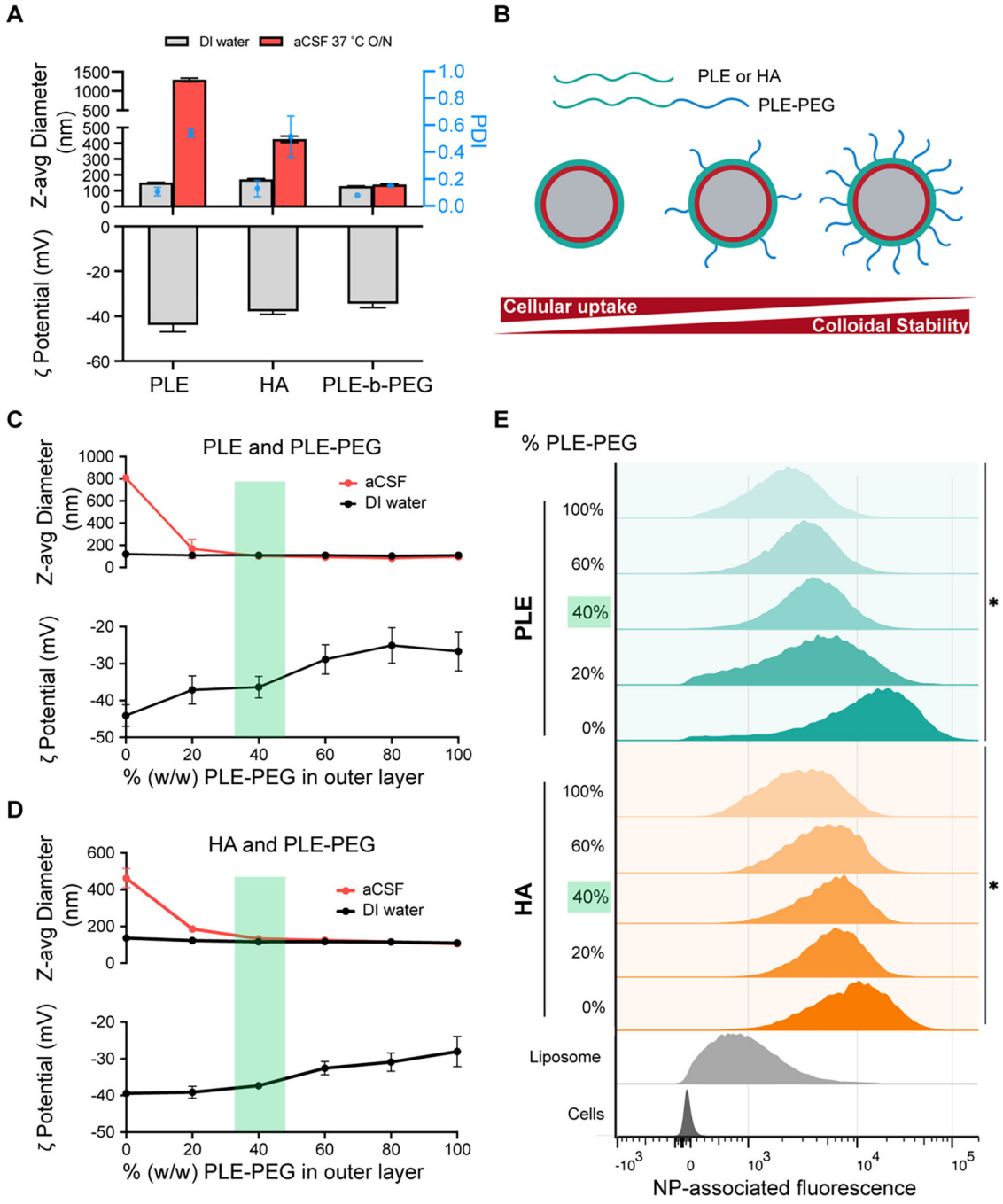

Figure 1: Co-layered LbL NPs balance colloidal stability with cellular associations.

A) Size, polydispersity, and zeta potential of LbL NPs with outer layers of poly-L-glutamate (PLE), sodium hyaluronate (HA), and poly-L-glutamate-b-PEG (PLE-PEG) measured using dynamic light scattering. All NPs display similar size and zeta potential when measured in DI water, but only PLE-PEG NP maintain their size in artificial cerebrospinal fluid (aCSF) after overnight incubation at 37 °C. **B)** Schematic showing the approach to balancing colloidal stability with cellular uptake by combining outer layer polyanions with PLE-PEG. **C, D)** NP characterization using dynamic light scattering of PLE (C) and HA (D) NPs

with different % (w/w) of PLE-PEG present during NP layering. The presence of 40% (w/w) PLE-PEG in the layering buffer is sufficient to form NPs that maintain colloidal stability in aCSF. **E)** Flow cytometry histograms showing the decreasing association of fluorescently-tagged NPs with GBM22 glioblastoma cells with increasing weight fractions of PLE-PEG in the outer layer. Histograms are pooled results from 3 technical replicates with * $p<0.05$ by one-way ANOVA. Error bars in panels A, C, and D represent the standard deviation from the arithmetic mean of three technical replicates.

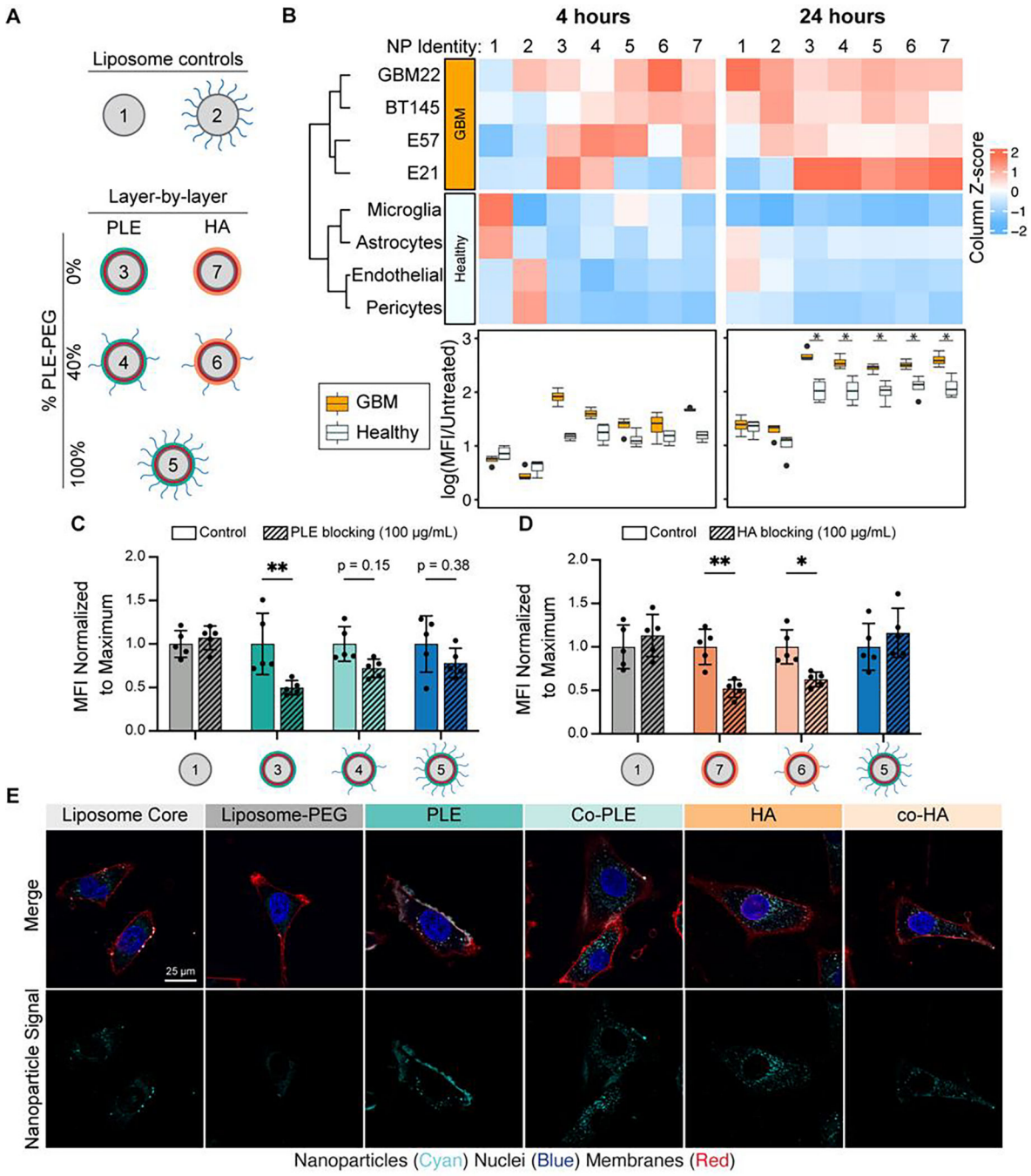

Figure 2: Co-layered LbL NPs maintain selective interactions with glioblastoma cells, leading to internalization.

A) Schematic of NPs used in NP-cell association studies. **B)** Column-normalized heat map of median fluorescence intensity values from flow cytometry after 4 and 24 hours of incubation. Hierarchical clustering reveals LbL NPs have specificity for glioblastoma cell lines over healthy cells *in vitro*. The lower box plot shows the overall NP-associated fluorescence for each formulation pooled over all cancerous and all healthy cell lines. * $p<0.05$ by Mann-Whitney U Test for non-parametric data with a false discovery rate of 0.05.

C, D) Relative flow cytometry association of NPs with and without exogenous PLE (C) or HA (D) to block interactions with cell membrane receptors. * $p<0.05$, ** $p<0.01$ by one-way ANOVA with Tukey post-hoc multiple comparisons. **E)** GBM22 cells were incubated with NPs for 24 hours and then fixed and analyzed by confocal microscopy. Relative to the liposome core, all LbL NPs showed substantially higher NP signal. PLE NPs were present mainly on the outer cell membrane, while HA and both co-layered formulations were internalized into the cytoplasm.

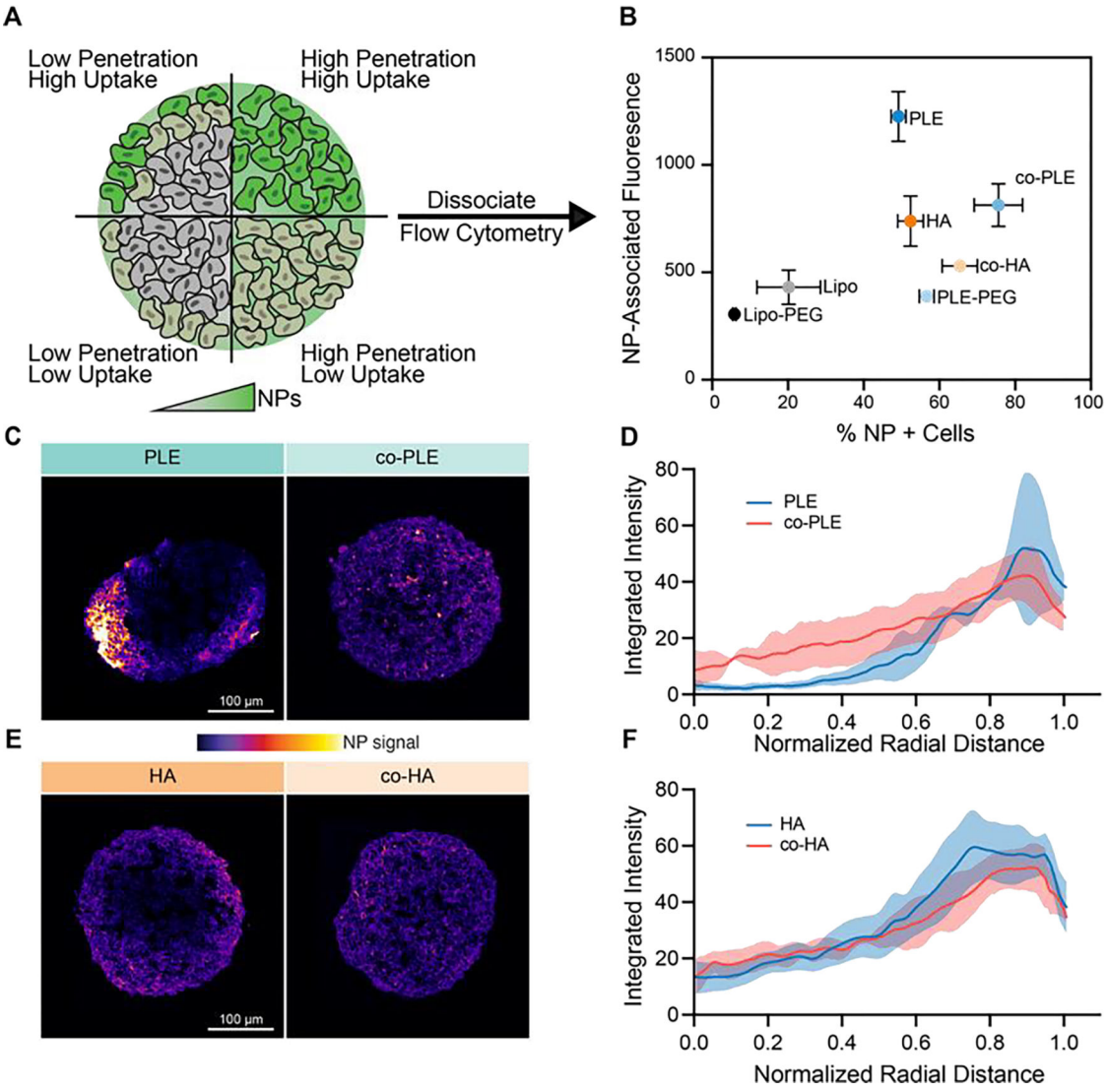

Figure 3: Co-layered LbL NPs penetrate 3D glioblastoma spheroids.

A) Schematic of flow cytometry assay used to measure the extent of NP uptake and penetration in spheroids. Nanoparticles are represented by green shading. **B)** After incubation with NPs, spheroids were dissociated into single cells and analyzed for percent NP-positive cells and their overall NP-associated fluorescence. Co-layered LbL NPs increase the fraction of NP+ cells compared to PLE and HA LbL NPs while increasing the NP-associated fluorescence compared to PLE-PEG NPs. **C)** BT145 spheroids were incubated with NPs for 24 hours, fixed, and cryosectioned into 10 μm sections for confocal microscopy. Representative cross-section shows that co-layered PLE NPs have more uniform penetration throughout spheroids than PLE NPs. **D)** Quantification of the radial average intensity as a function of distance from the spheroid center. **E, F)** Representative cross sections of spheroids incubated with either HA or HA/PLE-PEG NPs reveal no significant change in penetration. Shaded areas in panels D and E represent the standard deviation from the arithmetic mean of three technical replicates.

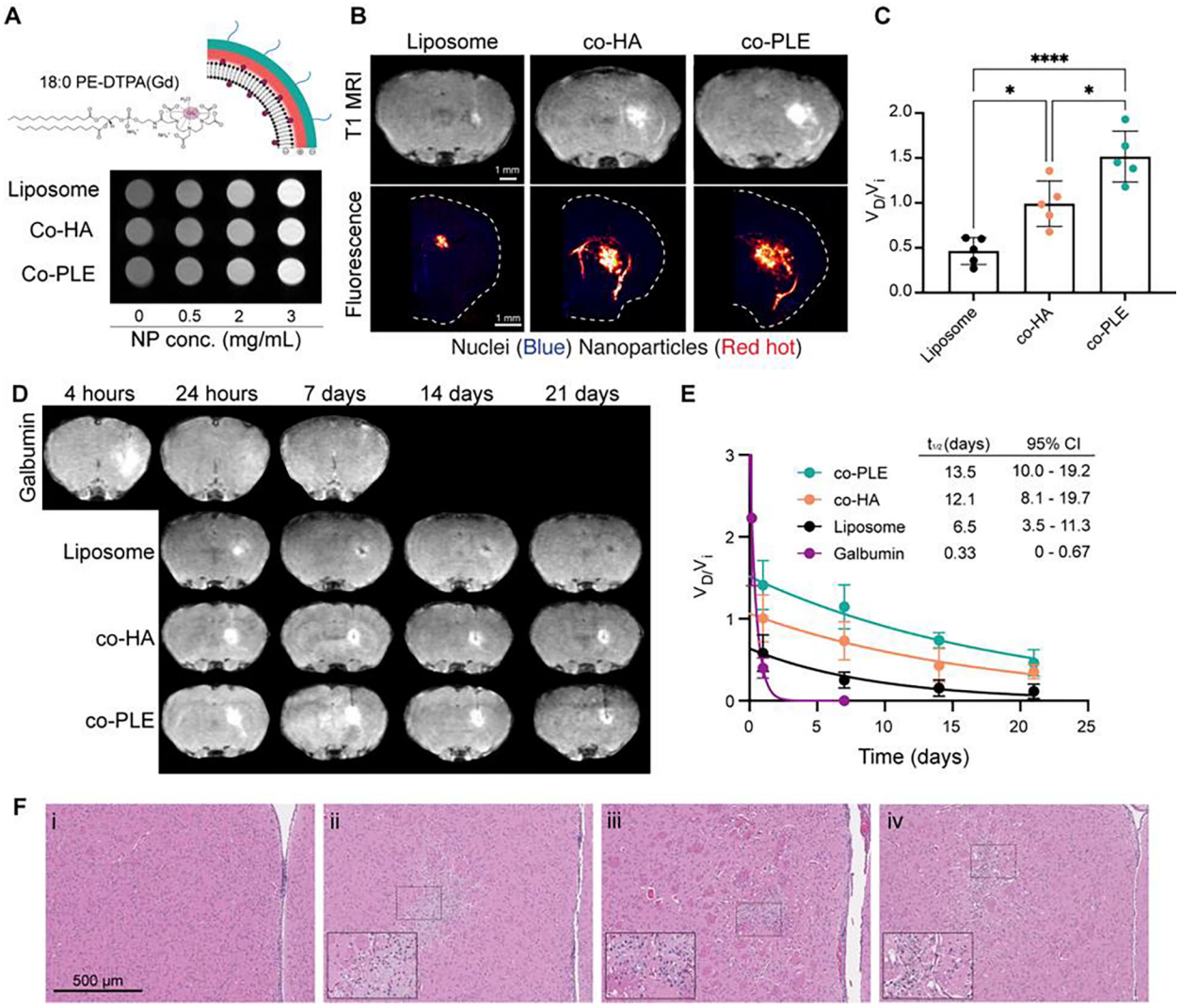

Figure 4: Co-layered LbL functionalization of Gd-functionalized liposomes increases distribution and retention following CED in healthy mice.

A) Top: Schematic showing the incorporation of 5 mol% 18:0 PE-DTPA(Gd) into the liposomal bilayer. Bottom: In-vitro MRI images of agarose phantoms with different concentrations of NPs, showing concentration-dependent T1 contrast. **B)** Top: T1-weighted coronal MRI images of healthy mice 24 hours after infusion with NPs. Bottom: Fluorescent micrographs of cryosectioned brains at approximately the same coronal plane as MRI images. **C)** Quantification of the segmented 3-D volume of NP T1 MRI contrast, expressed as a ratio of the volume of distribution (V_D) by the volume of infusion (V_I). Statistical analysis of n = 5 biological replicates was performed using one-way ANOVA with Welch's correction. **D)** T1-weighted coronal MRI scans of healthy mice showing the gradual loss of Gd-labelled albumin or NPs over 21 days. **E)** Quantification of the volume of distribution expressed as a ratio of V_D/V_I over 21 days. An exponential fit of V_D/V_I as a function of time for each group indicates that both LbL formulations have a longer lifetime than liposomes. A two-way mixed-effects model indicated a significant effect of time ($p<0.001$) and formulation on the volume of NP distribution ($p<0.001$). **F)** Haematoxylin and eosin

(H&E) staining of brains 21 days after administration of i) 5% dextrose, ii) liposomes, iii) co-PLE NPs, and iv) co-HA NPs. All NP groups showed trauma and focal necrosis at the needle tip, with infiltration of macrophages around the site of injection. Error bars in panels B, D, and E represent the standard deviation from the arithmetic mean of n = 6 biological replicates.

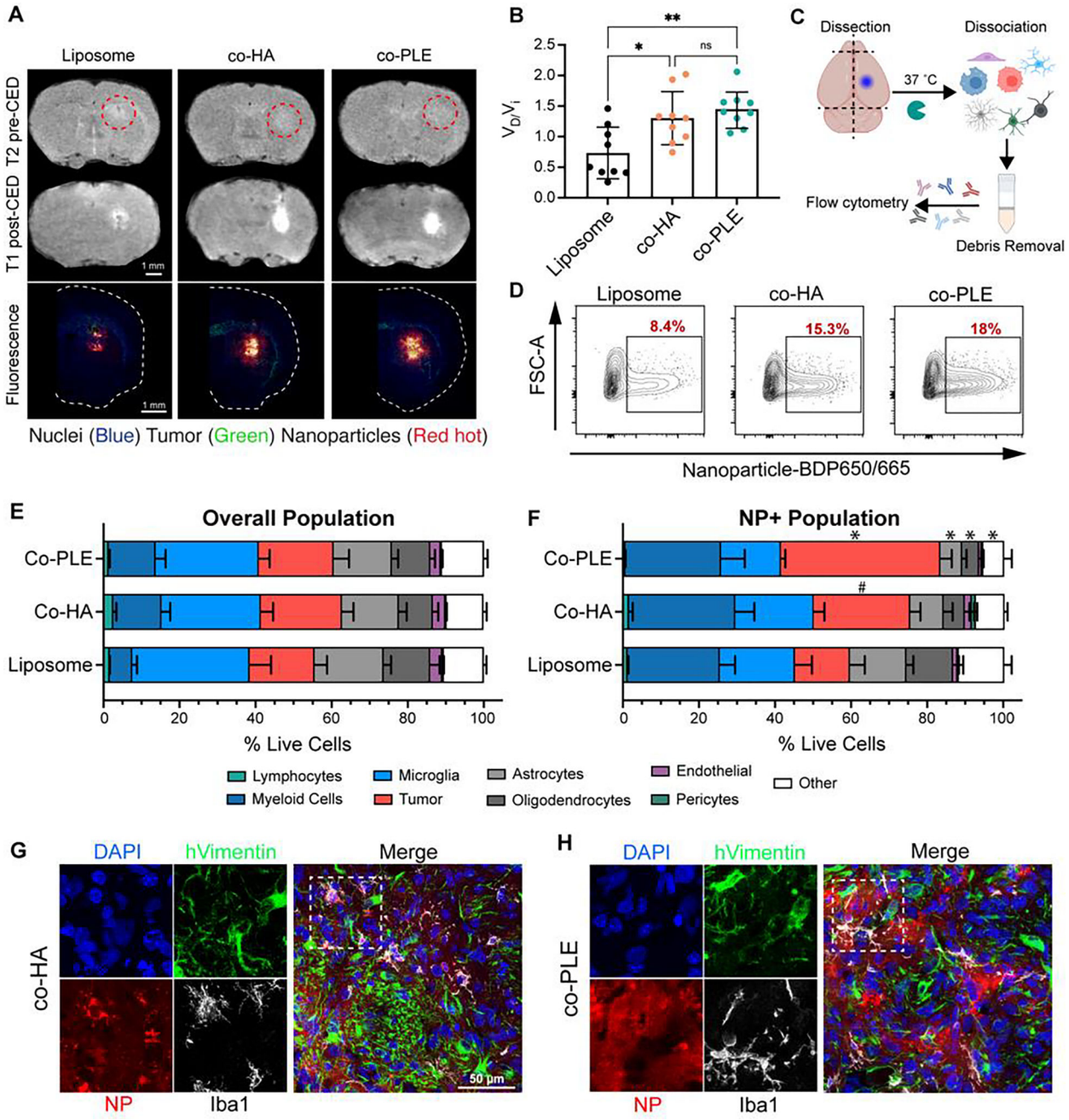

Figure 5: Co-layered LbL functionalization increases the volume of distribution and glioblastoma targeting following CED in tumor-bearing mice.

A) Top row: T2 weighted coronal MRI images of mice 24 hours before CED. Regions of T2 hyperintensity outlined in red circles represent the tumor bulk. Middle row: T1-weighted coronal MRI images of mice 24 hours after CED of NPs. Bottom row: Fluorescent micrographs of cryosectioned brains at approximately the same coronal plane as MRI images. **B)** Quantification of the segmented 3-D volume of NP T1 MRI contrast, expressed as a ratio of V_D/V_I. Error bars show the mean and standard deviation of n = 9 biological replicates. Statistical analysis was performed using one-way ANOVA with

Welch's correction. **C)** Schematic showing the preparation of mouse brain tissue for flow cytometric analysis of NP content. **D)** Representative flow cytometry histograms showing the NP-associated fluorescence in tumor cells. Percentages represent the portion of all tumor cells that were detected as NP-positive from pooled biological replicates. N = 6 for liposome and co-PLE NPs, n = 5 for co-HA NPs. **E)** Cellular composition of dissociated mouse brains from the different NP-treatment groups. **F)** Cellular composition of the fraction of cells that were first gated as NP+. Both LbL formulations show significant enrichment of the tumor cell population compared to the liposome group and overall population of live cells. Error bars show the mean and SEM for 6 biological replicates for liposomes and co-PLE and 5 replicates for co-HA. For each cell type, bars with a unique symbol are statistically significant from other NP groups (*$p < 0.05$, two-way ANOVA with Tukey post hoc test). **G, H)** Immunofluorescence of cryosectioned brain slices, showing myeloid cells and microglia in white (iba1), human tumor cells in green (hVimentin), nuclei in blue (DAPI), and NPs in red for co-HA (G) and co-PLE NPs (H).